# An off-line ion guide quadrupole mass spectrometer system

*Master's thesis: 15/9/2017*

*Author:*
Sara El Youbi

*First supervisor:*
Ilkka Pohjalainen

*Second supervisor:*
Iain Moore

JYVÄSKYLÄN YLIOPISTO
FYSIIKAN LAITOS

# Abstract

Sara El Youbi
An off-line ion guide quadrupole mass spectrometer system
Master's thesis
Department of Physics, University of Jyväskylä, 2017, 63 pages.

The commissioning of a new off-line ion guide quadrupole mass spectrometer (IGQMS) system, an off-line platform for the testing and development of new techniques to be implemented at the IGISOL– facility, is presented in this thesis. The differential pumping system is investigated and results of efficiency measurements of the front part of the system using a $^{223}$Ra alpha-recoil source are presented. Operational gas cell pressures from 1 up to 700 mbar have been demonstrated while maintaining operational pressure in the QMS chamber. A range of pressure measurements with different parameters is presented, and a transport efficiency through a squeezer-skimmer system of nearly 100 % has been measured.

Keywords: IGISOL, ion guide, mass spectrometer, off-line, vacuum, operational pressure, efficiency.

# Tiivistelmä

Sara El Youbi
Off-line ioniohjain kvadrupolimassaspektrometri systeemi
Pro Gradu -tutkielma
Fysiikan laitos, Jyväskylän yliopisto, 2017, 63 sivua.

Uuden erillisen ioniohjain-kvadrupolimassaspektrometri (IGQMS) -systeemin käyttöönotto on esitetty tässä työssä. Laitteisto on kehitetty uusien tekniikoiden testaamiseen ja kehittämiseen IGISOL–laitoksella. Työssä on tutkittu laitteiston differentiaalista pumpaussysteemiä ja laitteiston etuosan kuljetustehokkuutta käyttäen $^{223}$Ra alfa-rekyylilähdettä. Painemittausten tulokset eri parametreilla ovat esitetty. Kaasuohjaimen käyttöpainealue on mitattu olevan 1 ja 700 mbar:n välillä pitäen käyttöpaineen QMS kammiossa, ja skimmer-systeemin läpäisytehokkuus olevan lähellä 100 %.

Avainsanat: IGISOL, ioniohjain, massaspektrometri, off-line, tyhjiö, käyttöpaine, tehokkuus.

# Contents

# 1 Introduction

## 1.1 The IGISOL–facility

The Ion Guide Isotope Separator On-Line (IGISOL) facility, developed in the early 1980's at the University of Jyväskylä, is a chemically independent and fast method for the production of exotic radioactive ion beams. The method is based on the slowing down and thermalizing of products from nuclear reactions, originating from the impact of a primary beam delivered from either of two cyclotrons with a thin stable target, in helium gas, which is used as a stopping medium. The ions are transported out of the gas cell (often called ion guide) with the helium gas flow, guided in an static electric field through a SextuPole Ion Guide (SPIG) into the mass separator, where they are accelerated to a potential of 30 keV and separated using a magnetic field according to their mass over charge. The layout of the IGISOL–4 facility is shown in figure 1, illustrating the main experimental beam lines and scientific equipment, and a detailed overview of the IGISOL–technique can be found in [1].

The IGISOL–facility has a high demand for on-line experiments (in other words utilizing primary beams from the two cyclotrons) and often suffers from a lack of time for off-line testing and development. Thus, an independent off-line station, an off-line ion guide quadrupole mass spectrometer, has been developed to support the on-going experiments and to provide a test facility, the development and commissioning of which will be presented in this thesis.

## 1.2 The ion guide quadrupole mass spectrometer

The off-line ion guide mass spectrometer system is based on the IGISOL–method but differs in that it uses a quadrupole mass spectrometer (QMS) instead of a magnetic separator. Such a platform was first developed in 1990 at the University of Jyväskylä [2], but has not been in use since then. With the high demand for on-line measurement time at the IGISOL–facility, the idea for an off-line station has been resurrected in the last year. This research platform is referred to as a miniature IGISOL–facility and is called the "off-line rig" for simplicity.

The operation and testing of the off-line rig and the first measurements conducted with it are described in this thesis. Throughout the project, general construction and connections of the main components of the system were made, cabling to provide voltages, vacuum pump test-

ing and leak detection and estimations of base pressures in the vacuum chambers have been performed before conducting any experiments. The results of two studies are discussed in sections 5 and 6. In section 5, the behavior of the pressure in each chamber has been studied as a function of different parameters, from variation of the gas cell pressure and gas cell distance to the extraction system to variation of the exit hole size of the gas cell. This was done mainly to know the operational pressure range of the gas cell, which is restricted partly by the pumping capacity on the target (gas cell) chamber, and by the QMS chamber pressure, which houses an electron multiplier (EMT) detector. The experimental results have been compared with calculations of the throughput and conductance. Secondly, a study of the transport efficiency of radioactive ions through a squeezer-skimmer extraction system using a $^{223}$Ra alpha-recoil source is presented in section 6, and the initial results are discussed.

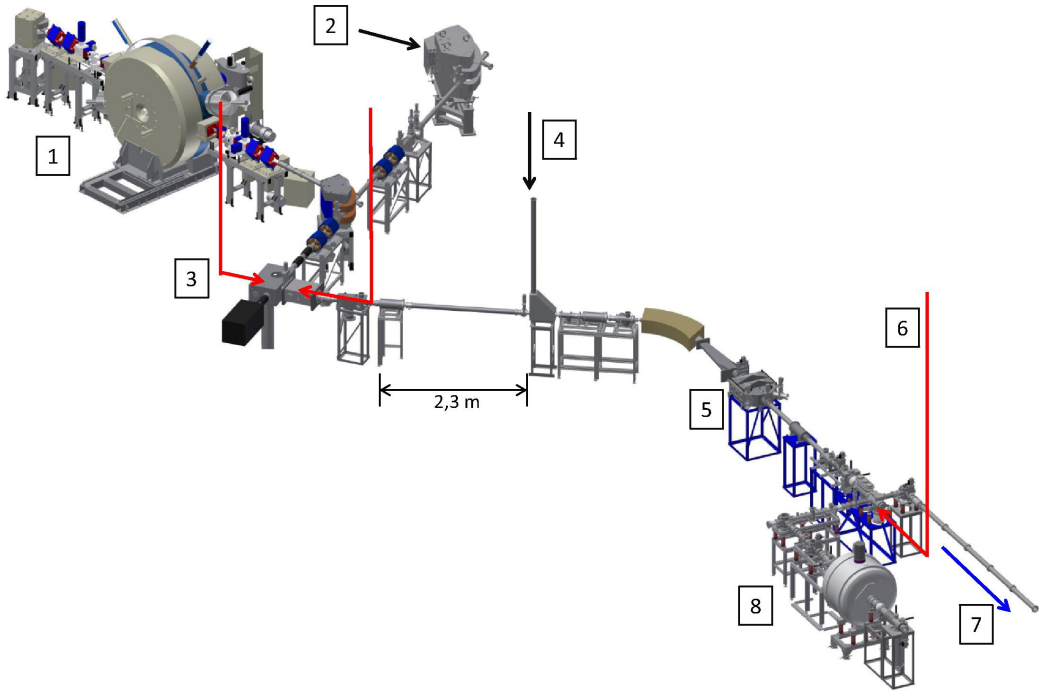


Figure 1: The layout of the IGISOL-4 facility [3]. The labels are as follows: 1. MCC30/15 cyclotron, 2. Beam delivery from the K = 130 MeV cyclotron, 3. Laser beam transport to the target area, 4. Vertical beam line for off-line ion source transport (discharge and surface ion sources), 5. Electrostatic switch-yard (spectroscopy line and new atom trap beam line are not shown), 6. Laser beam transport for optical manipulation in the radio-frequency (rf) quadrupole cooler and buncher, 7. Collinear laser spectroscopy beam line, 8. Penning trap facility.

# 2 Overview of the ion guide quadrupole mass spectrometer system

## 2.1 Three chamber configuration

The off-line ion guide quadrupole mass spectrometer (IGQMS), or "off-line rig" for short, consists of three main sections: the gas cell chamber, the ion optics for extraction and transport of ions and the QMS system for mass separation and ion detection. By means of a differential pumping system, each section is independently evacuated to provide the high vacuum required for the successful operation of the QMS and the electron multiplier (EMT) detector. Figure 2 shows a schematic of the IGQMS setup. A short description of the main chambers will be presented in the following.

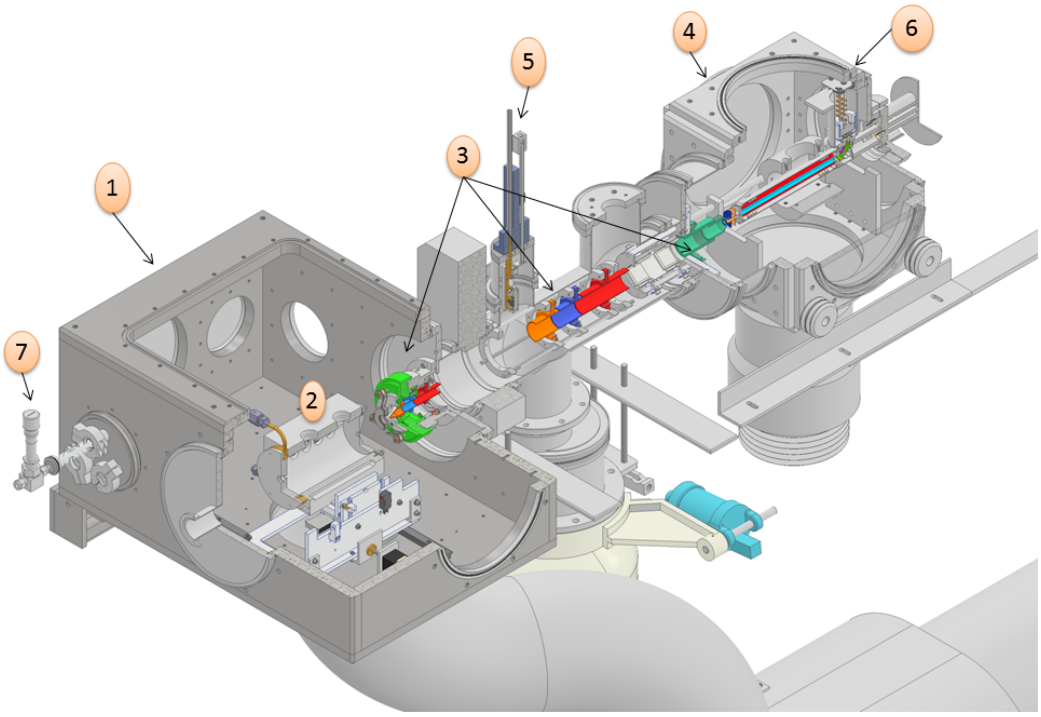


Figure 2: Schematic of the IGQMS setup, prepared using Autodesk Inventor software. The labels are as follows: 1. Gas cell (target) chamber, 2. Gas cell, 3. Ion optics, 4. QMS chamber, 5. Si detector, 6. EMT detector, 7. Gas inlet.

### 2.1.1 Gas cell

The ion production and extraction happens within the gas cell chamber. Ions are created inside a gas cell filled with either helium or argon, and are extracted from the cell within the buffer gas which is evacuated through an exit nozzle of $\approx$1 mm diameter. Helium or argon are typically the gases of choice, since they are inert and have high ionization potentials (which leads to ion survival of the species of interest).

Different gas cell geometries are used depending on the nuclear reaction mechanism. For example, fission fragments produced via charged particle-induced fission are extracted by large volume fission ion guides and fusion-evaporation products either by light- or heavy-ion guides. An overview of the different gas cells in use at the IGISOL–facility and the historical development of them can be found in [4].

Two different gas cells were used in the experiments described in this thesis. First measurements were conducted with a (californium, Cf) gas cell on loan from KU Leuven, Belgium, shown in figure 3. It consists of a 100 mm inner diameter and 100 mm length chamber (volume, V = 0.79 l), different exit holes of 0.5, 0.9 and 1.2 mm diameter and feedthroughs for electric current for the heating of stable filaments (which were not used). This gas cell was designed to house a spontaneous $^{252}$Cf fission source, however in this work such a source was not required. The second set of measurements were conducted using a smaller volume gas cell which was designed for actinide studies [5], a cubic shaped cell with dimensions 6.0x4.4x7.2 cm (which can be approximated to a cylinder of 30 mm diameter and 50 mm length, V = 0.035 ml) shown in figure 4.

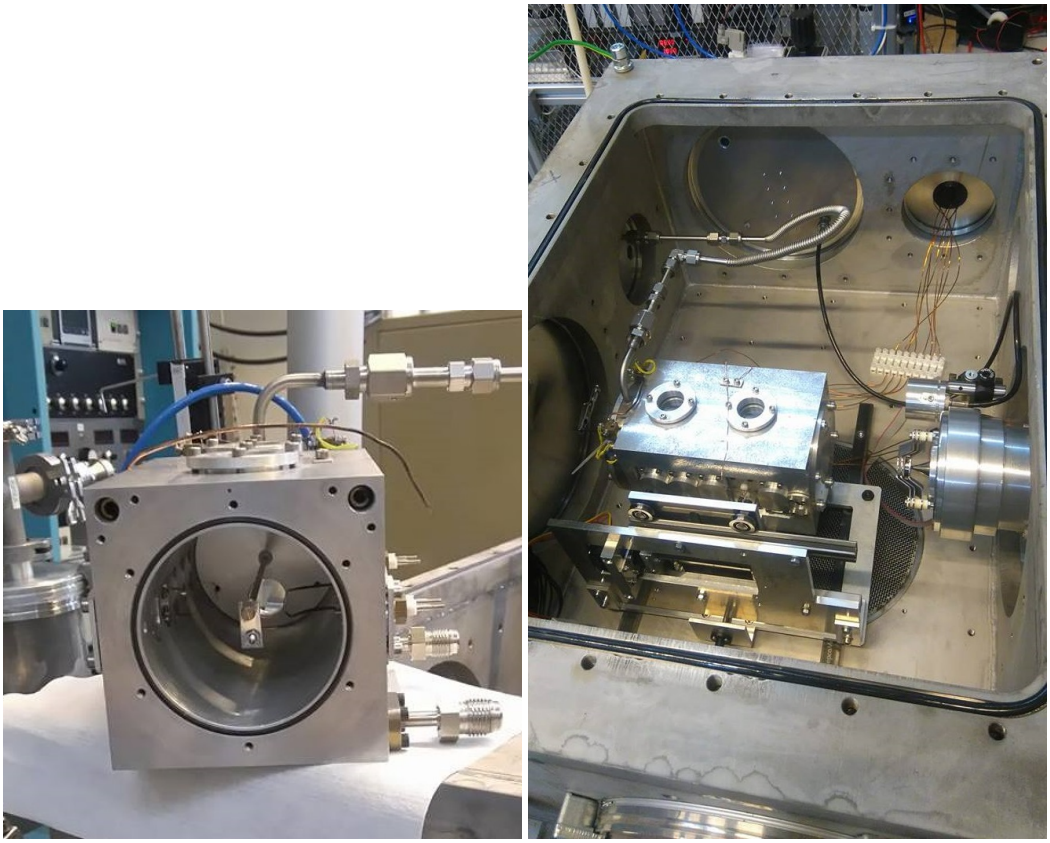

Figure 3: Photographs of the Cf gas cell. *Left* : Photograph of the Cf gas cell with the view looking into the chamber without the exit flange attached. Feedthroughs for gas and water cooling are seen on the right upper corner and the mounting for the $^{223}$Ra alpha-recoil source described in section 6 is visible in the middle. *Right* : Photograph of the Cf gas cell mounted inside the gas cell chamber. The squeezer and skimmer electrodes mounted on a barrel are seen on the right. Ions extracted from the gas cell are guided through these electrodes into the second chamber.

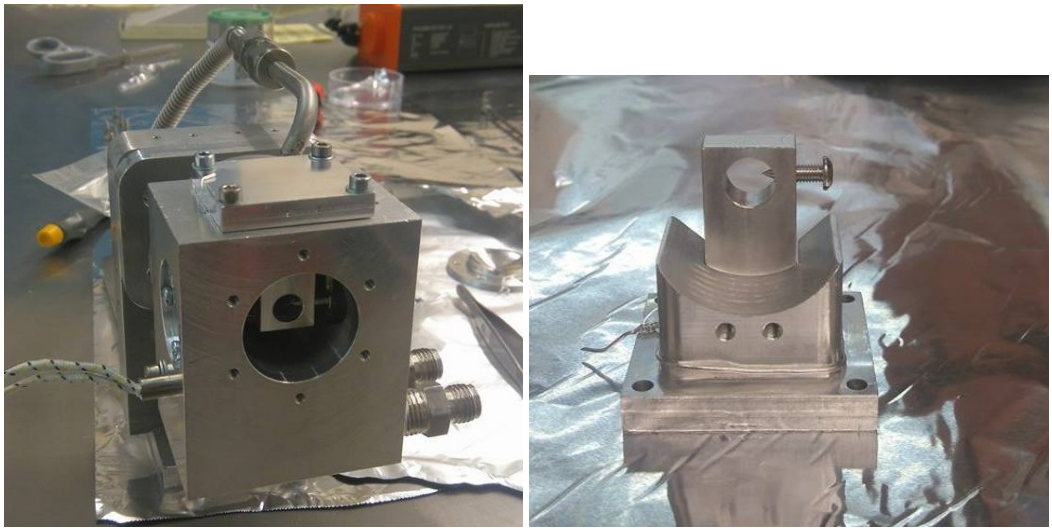

Figure 4: Photographs of the actinide gas cell. *Left* : Photograph of the actinide gas cell, with the $^{223}$Ra source inside. The exit flange has been removed. *Right* : Photograph of the $^{223}$Ra source which is implanted on the top of a needle. The whole structure mounts onto the actinide gas cell.

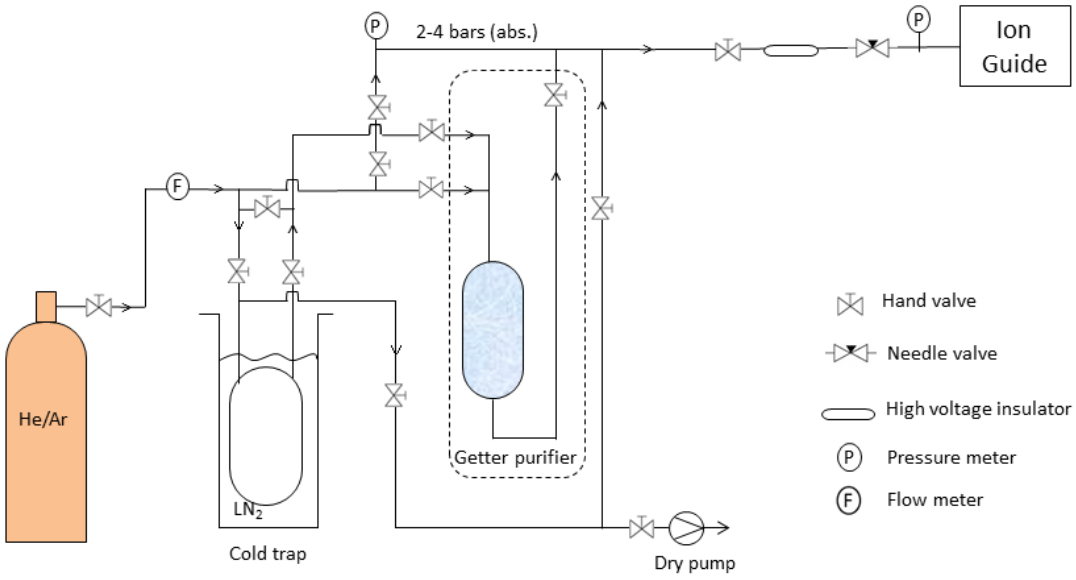


Figure 5: Schematic of the gas handling system.

The purity of the buffer gas, He or Ar, is crucial for the efficiency of the gas cell. Impurities in the buffer gas at the level of parts-per-million lead to molecular formation, which reduces the efficiency of atomic ion extraction. Preventing these losses requires impurity levels of sub-parts-per-billion (ppb) [6]. To achieve such high purity conditions, a gas purification system is needed. Figure 5 shows a schematic of the gas handling system, similar to the one used in the IGISOL-4 facility [6]. The buffer gas is regulated from gas bottles to 2-4 bars and is fed through the purification stage which consists of a liquid nitrogen cooled cold trap filled with zeolite 13-X. A getter purifier can be added for further purification. However, it was not included in this work. The main impurities, $H_2O$, $N_2$ and $O_2$, are removed from the helium gas via deposition on the high surface area zeolite material. The zeolite material can be regenerated by baking of the cold trap while pumping the gas lines using the dry pump indicated in figure 5.

The needle valve regulates the pressure of the purified helium or argon entering the gas cell. At the IGISOL–facility, gas cells operate typically at 200-300 mbars. We tested much higher pressures with the off-line rig (up to $\approx$900 mbars).

### 2.1.2 Ion optics

The ion optics system plays an important role in mass spectrometers in order to achieve good sensitivity in the QMS device. It steers and focuses ions from the ion source into the quadrupole mass filter with electric and magnetic fields.

The ion optics used in the extraction system of the off-line rig, shown in figure 6, consists of three squeezer plates (or electrostatic lenses), a skimmer electrode and two Einzel lenses, which are suitable for low-energy ion beams (<100 eV). An Einzel lens is an electrostatic optical element which focuses the beam without changing its energy. It consists of three cylindrical lenses electrically isolated from each other.

The skimmer electrode with a squeezer electrode system around it is mounted between the gas cell and the Einzel lens in order to achieve maximum ion transmission (and to prevent the neutral buffer gas from entering the mass separator). Figure 6a presents a CAD model of the skimmer and squeezer optics. The skimmer has thin walls with cylindrical symmetry and a sharp orifice edge of $d = 1.03$ mm diameter. Heavier ions pass through the skimmer while helium gas is pumped (skimmed) away. The squeezer electrodes act to "squeeze" the ions through the skimmer with the aid of the gas flow.

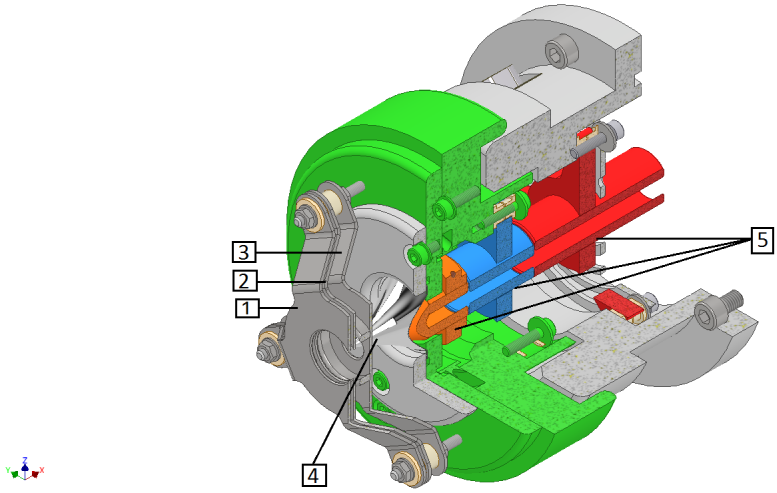


(a) Squeezer plates (1-3), skimmer electrode (4) and smaller Einzel lens (5).

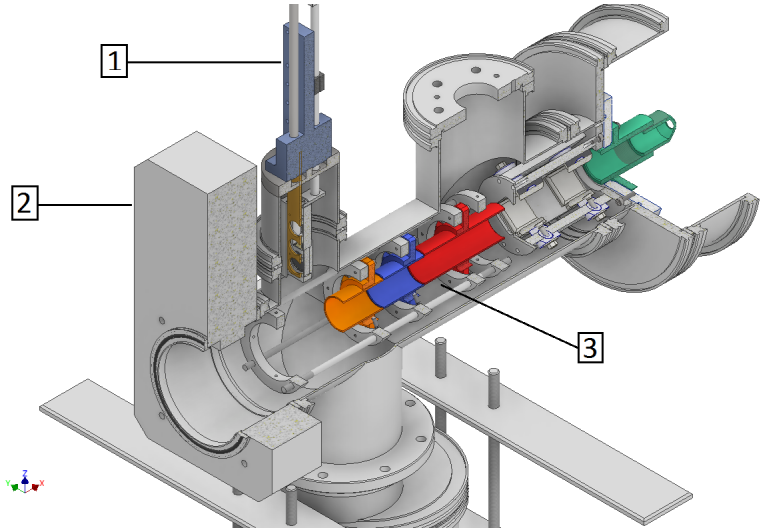


(b) Bigger Einzel lens.

Figure 6: CAD model of the ion optics system in the second vacuum chamber (extraction chamber), before the QMS chamber. A Si detector (1) is mounted just after the gate valve (2) which separates the gas cell chamber from the extraction chamber. Following this are a series of Einzel lenses (3) used to guide and focus the ions to the entrance of the QMS chamber (not shown).

### 2.1.3 The quadrupole mass filter

The quadrupole mass spectrometer was invented in 1953 by Paul and Steinwedel [7] and is nowadays widely used, for example in residual gas analysis, since its basic function is to select ions having different $m/q$ ratios. The quadrupole mass filter is unique in that it uses the motion of ions in alternating and static electric fields without magnetic fields. It consists of four parallel metal rods inside a vacuum chamber positioned as shown in figure 7. In order to obtain ideal quadrupole fields, hyperbolic rods are required. In practice however, real analyzers use cylindrical rods.

An electric field is created within the quadrupole by applying direct current voltage $U$ and high-frequency alternating voltage $Vcos(\omega t)$ to opposing pairs of rods with opposite polarities. Using the cartesian coordinate system and assuming the axis of the rod array to lie along the z-axis, then one pair of rods lies on the x-axis while the other pair on the y-axis. Only ions of a certain mass-to-charge $m/q$ ratio for a given DC and AC voltage ratio are transmitted. There are two methods for filtering the ions: varying $U$ and $V$ and keeping their ratio $U/V$ constant for a constant angular frequency $\omega$, or varying the angular frequency $\omega$ and keeping $U$ and $V$ constant.

The motion of ions through the quadrupole is described by so-called Mathieu equations, which are derived from Newton's equations of motion $F = qE$, where $q$ is the charge of the ion and $E$ the electric field. The Mathieu equations are solved numerically and a detailed description of their applications can be found in the paper by M. Sudakov [8].

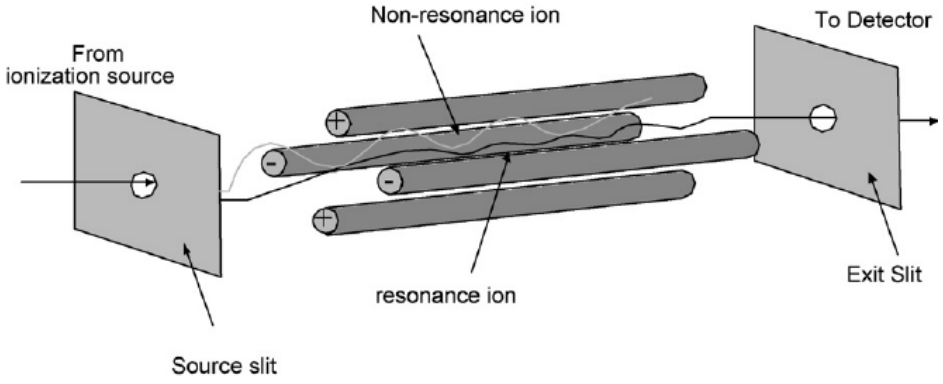


Figure 7: Schematic of a quadrupole mass filter [9].

The motion of an ion in $x-$, $y-$ and $z-$direction is given by the fol-

lowing equations, which are examples of Mathieu equations,

$$\begin{aligned}
\frac{d^2x}{dt^2} &= -(\frac{e}{mr_0^2})(U - Vcos\omega t)x, \\
\frac{d^2y}{dt^2} &= (\frac{e}{mr_0^2})(U - Vcos\omega t)y, \\
\frac{d^2z}{dt^2} &= 0,
\end{aligned} \tag{1}$$

where $U$ is the DC voltage, $V$ the RF voltage, $\omega$ the RF frequency, $t$ the time, $r_0$ the field radius (effective radius between electrodes), $e$ the elementary charge and $m$ the ion mass. These variables are combined into three parameters $a_u$, $q_u$ and $\xi$ as follows

$$\begin{aligned}
a_u = a_x = -a_y &= \frac{4eU}{m\omega^2 r_0^2}, \\
q_u = q_x = -q_y &= \frac{2eV}{m\omega^2 r_0^2}, \\
\xi &= \frac{\omega t}{2}.
\end{aligned} \tag{2}$$

Thus, the equations of motion (1) are reduced to the general form of the Mathieu equation

$$\frac{d^2u}{d\xi^2} + (a_u - 2q_u cos2\xi)u = 0, \tag{3}$$

where $u$ represents the displacement. This equation has analytic solutions for an infinite quadrupole length. For finite lengths, equation 3 requires numerical solution. Ions pass through the quadrupole only if the x- and y-motions are stable. Figure 8 shows the stability diagram, known as the Mathieu diagram, representing the stability in both directions for an infinite filter length. The ratio $a_u/q_u = 2U/V$ gives the load line of the filter, also called the operating or scan line. The area bounded by the curves is called the stability triangle, which represents the stable trajectories of ions oscillating with amplitudes $r < r_0$. The peak of the stability region is at $a_{u,p} = 0.237$ and $q_{u,p} = 0.706$, thus the quadrupole filters ions with $U/V = a_u/2q_u < 0.1678$.

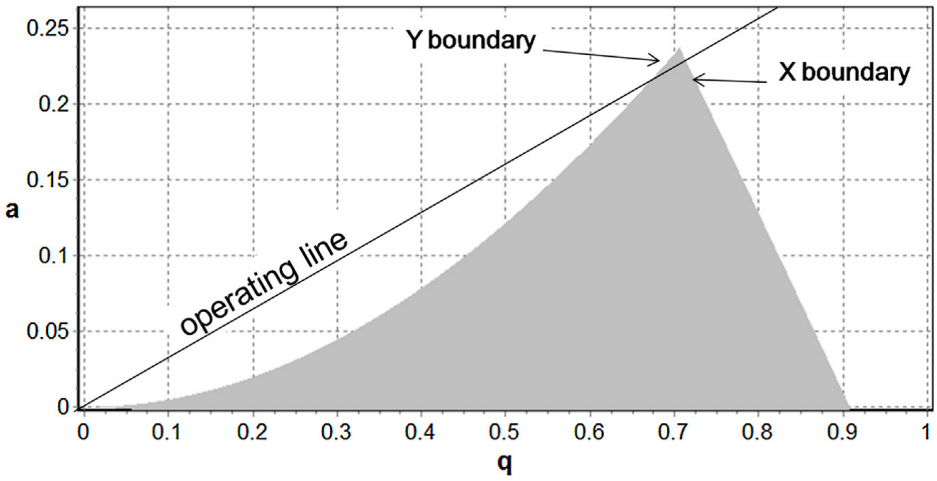


Figure 8: Mathieu diagram [8].

In the IGQMS, the separated ions are detected either directly by a silicon detector or a Faraday cup, or by an electron multiplier (EMT) detector after being deflected by $90^0$. The EMT detector is visible in the schematic drawing of figure 2.

# 3 Throughput and Conductance

In order to estimate the background pressure in the different chambers, a calculation of the conductance of connections between the chambers and pumps is needed.

The gas inside a chamber at air pressure is initially in a viscous state. Because of the high number of collisions the gas flow in this state is collective hence the term viscous. When evacuating the chamber to lower pressures, the gas state transfers through an intermediate state (Knudsen's state and flow) to a molecular state, where the motion of molecules is independent from each other and the flow is called molecular. Figure 9 shows the relationship between pipe diameter and pressure in different flow regimes.

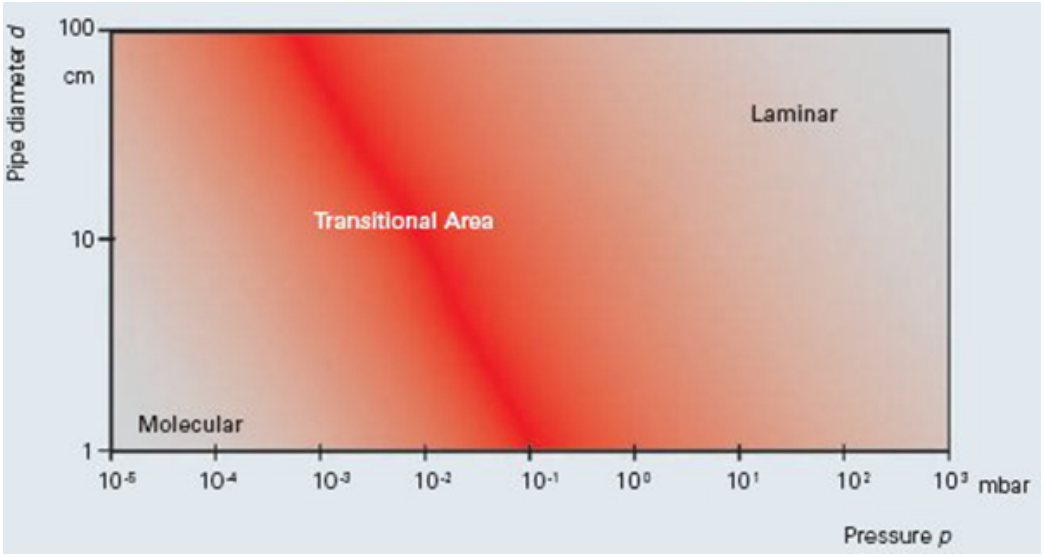


Figure 9: Pipe diameter and pressure in different flow regimes [10].

The pumping of gas, i.e. the flow rate of the gas, is described by the throughput $Q$, in mbar.l/s, as

$$Q = \frac{d(PV)}{dt} = P\frac{dV}{dt} = PS, \tag{4}$$

where $P$ denotes the pressure in the chamber in mbar, $V$ the gas volume in liters and $S$ the pumping speed in l/s. The throughput depends on the pressure difference between the chambers and the geometry of the connection between them. The geometry dependence is defined by the conductance, and is expressed as

$$C = \frac{Q}{\Delta P} = \frac{Q}{(P_2 - P_1)}. \tag{5}$$

In his book, Vacuum Technology [10], Roth describes the throughput of a gas through an aperture, from a volume with high pressure $P_0$ to a volume with lower pressure $P_1$, by

$$Q = 0.052 d^2 P_0 \sqrt{\frac{T}{A}}, \tag{6}$$

where $d$ is the exit hole diameter in mm, $P_0$ the gas cell pressure in mbar, $T$ the temperature in Kelvin and $A$ the molar mass of the buffer gas in g/mol.

The conductance in each flow regime is different and depends on the geometry of the connections between chambers and pumps (aperture, tube, pipe...).

The conductance of a pipe of diameter $d$ and length $l$ in viscous flow is given by [10]

$$C_{v,p} = \frac{\pi d^4}{1.28 \cdot 10^5 \eta l} \frac{p_1 + p_2}{2}, \tag{7}$$

with $p_1$ and $p_2$ the pressures at the entrance and the exit of the pipe respectively and $\eta$ the dynamic viscosity, which at 300 K is $1.9879 \cdot 10^{-7}$ mbar.s for helium and $2.2721 \cdot 10^{-7}$ mbar.s for argon.

The conductance in molecular flow is [10]

$$C_{m,p} = 3.81 \sqrt{\frac{T}{A}} \frac{d^3}{l}, \tag{8}$$

where $T$ is the stagnation temperature of the gas in Kelvin, $A$ the molar mass of the gas in g/mol, and $l$ and $d$ the length and diameter of the pipe in cm.

Combining the last two equations gives rise to a formula for conductance in all regimes:

$$C_p = \frac{\pi d^4}{960 \eta l} \frac{p_1 + p_2}{2} + 3.82 \sqrt{\frac{T}{A}} \frac{d^3}{l} \Big[ \frac{1 + 1.46 \cdot 10^{-2} \sqrt{\frac{A}{T}} \frac{d(p_1+p_2)}{2\eta}}{1 + 1.81 \cdot 10^{-2} \sqrt{\frac{A}{T}} \frac{d(p_1+p_2)}{2\eta}} \Big]. \tag{9}$$

The conductance of an aperture in a viscous state is given by [10]

$$C_{v,a} = 6.6216 S \sqrt{\frac{T}{A}}, \tag{10}$$

and in the molecular flow [10] by

$$C_{m,a} = 3.64 S \sqrt{\frac{T}{A}}, \tag{11}$$

where $S$ is the area of the aperture in $\mathrm{cm}^2$, $T$ the temperature in Kelvin and $A$ the molar mass of the gas in $\mathrm{g.mol}^{-1}$. With these units, the conductance is in $\mathrm{l.s}^{-1}$.

For air at room temperature 20°C $\sqrt{\frac{T}{A}} = 3.181$, therefore equation 11 takes the form of [10]

$$C_{air} = 11.6 S. \tag{12}$$

Vacuum systems are often comprised of many elements, connected in series or in parallel. The total conductance for elements $(C_i)$ connected in series is calculated by

$$\frac{1}{C_{tot}} = \frac{1}{C_1} + \frac{1}{C_2} + \frac{1}{C_3} + ... = \sum \frac{1}{C_i}, \tag{13}$$

and when connected in parallel by

$$C_{tot} = C_1 + C_2 + C_3 + ... = \sum C_i. \tag{14}$$

Table 1 lists the calculated conductances of the apertures used between each chamber of the off-line rig for helium and argon (eq. 11), and air (eq. 12). Later, in section 4.3, table 3 lists the conductances of pipes and apertures through which each chamber is pumped and the effective pumping speed in each chamber, described in the next section.

| | Aperture diameter (mm) | Buffer gas | | |
|---|---|---|---|---|
| | | He 4.003 g/mol | Ar 39.95 g/mol | air 28.97 g/mol |
| Conductance $C_{1-2}$ l/s | $D_{1-2}$=3.9 (without skimmer) | 3.76 | 1.19 | 1.38 |
| | $D_{1-2}$=1.03 (skimmer) | 0.26 | 0.08 | 0.10 |
| Conductance $C_{2-3}$ l/s | $D_{2-3}$=12 | 35.62 | 11.27 | 13.07 |

Table 1: Conductance of apertures, between gas cell chamber and lens system ($C_{1-2}$), and between lens system and QMS chamber ($C_{2-3}$), for helium, argon and air. Two different aperture diameters are used between chamber 1 and 2, the first (3.9 mm) represents the aperture between the two chambers without the skimmer whereas the second (1.03 mm) represents the skimmer.

The QMS chamber is pumped via an aperture of diameter $d = 160$ mm and its conductance is calculated using eq. 11, whereas the lens system is pumped via a pipe of length $l = 100$ mm and diameter $d = 100$ mm and the conductance is thus calculated with eq. 8.
The gas cell chamber is pumped via an S-shaped cylindrical pipe, which makes its conductance calculation difficult. Therefore, the shape has been simplified for calculations to three cylindrical pipes perpendicularly connected with two elbows. A grid is mounted between the gas cell chamber and the tube, which decreases the area of the aperture by approximately 10 %. Roth [10] gives a formula for the conductance of an elbow of length $l_1$ and $l_2$

$$C_{elbow} = 3.81\sqrt{\frac{T}{A}}\frac{d^3}{l_1 + l_2}. \tag{15}$$

Taking into account all of the factors and simplifications mentioned above, the conductance of the S-shaped tube $C_s$ can be estimated using eq. 8, 11 and 13 as

$$\frac{1}{C_s} = 2\frac{1}{C_{elbow}} + \frac{1}{C_{m,a}} \tag{16}$$

or

$$\frac{1}{C_s} = \frac{1}{C_{m,p1}} + \frac{1}{C_{m,p2}} + \frac{1}{C_{m,p3}} + \frac{1}{C_{m,a}}. \tag{17}$$

The dimensions of the estimated three pipes are $d_1 = 219$ mm $l_1 = 190$ mm, $d_2 = 219$ mm $l_2 = 600$ mm and $d_3 = 219$ mm $l_3 = 190$ mm, and the dimension of the elbows are $d_{elbow} = 219$ mm $l_1 = 190$ mm and $l_2 = 300$ mm. The area of the aperture of $d_{ap} = 219$ mm diameter is decreased by 10 % by the grid $C_{grid} = 0.1C_{ap}$. Therefore, equation 17 gives $C_s = 2724$ l/s for helium.

# 4 Pumping system

It is important to have the background pressure within the chambers as low as possible in order to minimize the probability of collisions with the background gas, and to provide the required low pressure ($< 10^{-5}$ mbar) for the functioning of the EMT detector. Figure 10 shows a schematic of the differential pumping system. The gas cell chamber is connected to a roots pump, the ion optics chamber to a diffusion pump and the QMS chamber to a turbo pump with necessary backing pumps. A short description of the different pumps used is presented next.

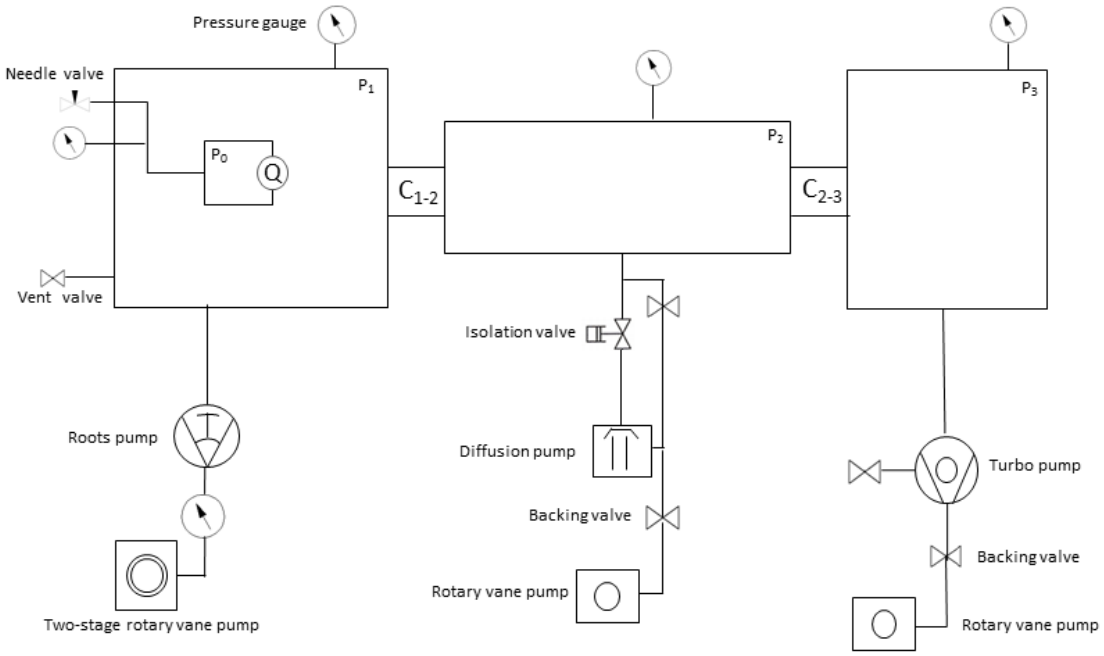


Figure 10: Schematic of the pumping system.

## 4.1 Roots vacuum pump

Roots pumps are dry vacuum pumps able to pump high volumes of gas. They consist of two symmetrical rotors with an eight-shape configuration rotating in opposite directions without contact. Roots pumps require backing pumps, for example rotary vane pumps. A more detailed explanation of the working principle of roots pumps can be found in [11].

An Edwards EH4200 roots pump, with pumping speed $\approx 4200$ m$^3$/h, is used to pump down the pressure of the gas cell chamber to $10^{-4}$ mbar and an Edwards E2M275 rotary vane pump is used as a backing pump. The pumping speed of the roots pump with the backing is 3100 m$^3$/h [11].

## 4.2 Diffusion pump

Diffusion pumps are commonly used in mass spectrometry in high vacuum range ($10^{-9}$ mbar). They use the vapor of a boiling fluid, usually oil, to capture air molecules. They consist of three cone-shaped pressure jets, decreasing in size as one moves upwards. When the heated fluid in the

bottom evaporates, the gas moves upwards and exits from the pressure jets at a downward angle. The gas vapor traps air molecules (through diffusion) and converts to liquid when it reaches the water-cooled chamber walls. The air molecules are then released at higher pressure and the oil runs down the walls to the bottom and the cycle begins again. A more detailed description of the working principal of diffusion pumps can be found in [12].

The ion optics chamber is pumped down to $10^{-5}$ mbar using an Edwards Diffstak 160 diffusion pump, which has a pumping speed of 1000 l/s. An Edwards RV3 rotary vane pump is used as a pre-vacuum pump.

## 4.3 Turbo pump

Turbo molecular pumps consist of pairs of rotating rotor blades and stationary stator blades. The working principle is based on the transfer of the rotor blades mechanical energy into momentum of the gas molecules. The gas molecules hit the angled rotor blades and pass through holes in the stator blades towards the next rotor blade, where collisions occur again. The gas molecules are transferred through the same process down each pair of blades until exiting from the exhaust.

Turbo molecular pumps work in molecular flow conditions and thus require backing pumping. A scroll pump is used as such a backing pump, connected to an Edwards EXT 500 turbo pump in order to evacuate the QMS chamber to less than $10^{-6}$ mbar.

## 4.4 Effective pumping speed

Table 2 lists the pumping speed and compression ratio for all the vacuum pumps used. The compression ratio $K_0$ describes the maximum ratio between the exhaust $p_{outlet}$ and intake $p_{inlet}$ pressure and is expressed as follows:

$$K_0 = \frac{p_{outlet}}{p_{inlet}}. \tag{18}$$

The higher the compression ratio the higher the pumping speed and thus the shorter the time required to pump down to an appropriate vacuum.

In order to calculate the compression ratio of the roots pump, the inlet and outlet pressure was measured as a function of gas cell pressure, using helium as buffer gas. Figure 11 shows a plot of the measured values, where $P_1$ illustrates the outlet pressure and $P_2$ the inlet pressure. A linear fit was applied to each set of data points, and the compression ratio with

errors was calculated from the slope values using eq. 18, resulting in $K_{0,roots} = 13.9$, which lies within the range given by the manufacturer (10 to 50, see table 2).

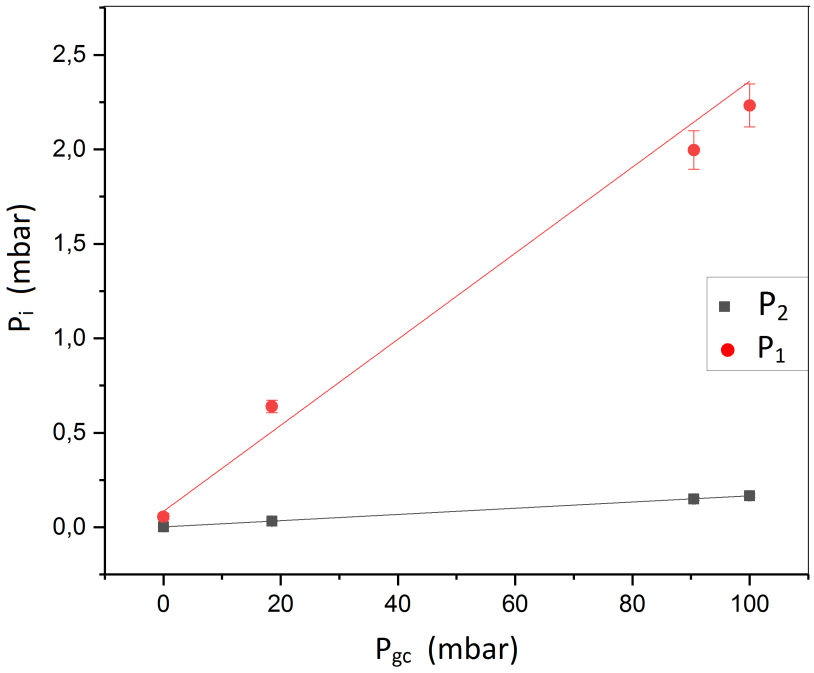


Figure 11: Inlet (solid squares, $P_2$) and outlet (solid circles, $P_1$) pressure as a function of gas cell pressure $P_{gc}$.

| Technical data | Unit | EH4200 Roots pump | E2M275 rotary vane pump | Diffstak 160 Diffusion pump | RV 3 rotary vane pump | EXT 500 Turbo pump | XDS 5 dry scroll pump |
|---|---|---|---|---|---|---|---|
| Pumping speed (He) | l/s | 861 | 70.839 | 875 | 0.91674 | 580 | 1.33344 |
| Compression ratio | | 10 to 50 | $1.013 \times 10^6$ | $10^9$ | 2 | $10^8$ | 2 |

Table 2: Performance data for the used vacuum pumps [11–13].

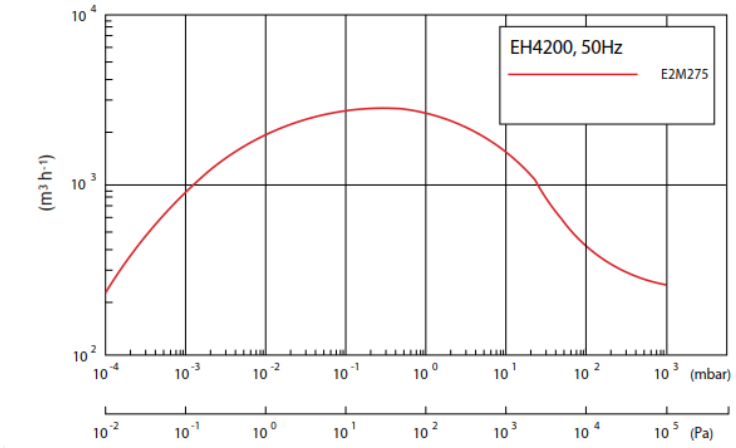


(a) Pumping speed characteristic of EH4200 roots pump [11].

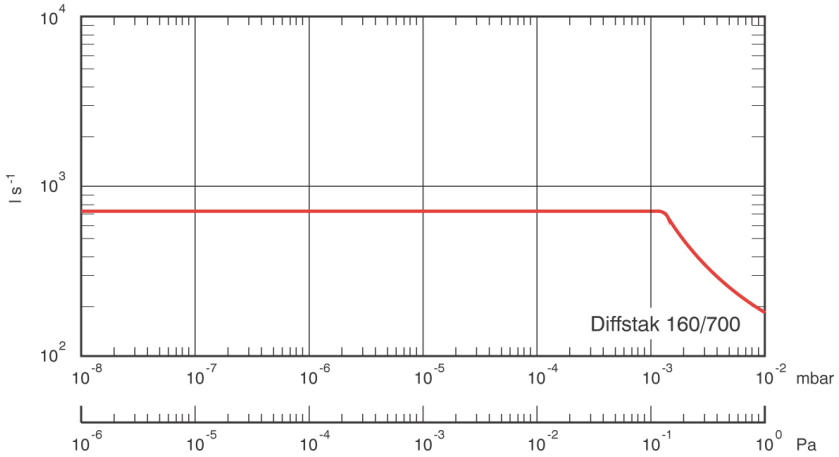


(b) Pumping speed characteristic of Diffstak 160 diffusion pump [12].

Figure 12: Performance curve of roots pump and diffusion pump.

Each vacuum pump has an application range, which describes how the pumping speed of the pump varies with pressure, presented as a pumping speed vs pressure curve as seen in figure 12. Such figures describe the pump's performance throughout its probable application range, allowing users to assess the pump's capability at specific operating conditions for different gases. Figure 12 shows the performance curve of the used diffusion and roots pump. For example, in the case of the diffusion pump, figure 12b, at pressures higher than $\approx 1.5 \cdot 10^{-3}$ mbar the pumping speed decreases, which then leads to an increase in the chamber pressure.

The conductance $C$ connecting the pump to the chamber reduces the pumping speed of the pump $S$ to an effective pumping speed $S_{eff}$, which is calculated by

$$S_{eff} = S\frac{C}{S+C}. \tag{19}$$

Table 3 lists the conductances of the connections through which the chambers are pumped, calculated in the previous section, and the normal and effective pumping speed in each chamber. The effective pumping speed values were used in the pressure calculation in section 5.

| Chamber | Conductance l/s | | | Effective pumping speed l/s | | Normal pumping speed l/s | |
|---|---|---|---|---|---|---|---|
| | He | Ar | air | He | Ar | He | Ar |
| Gas cell chamber | 2724 | 862 | 1013 | 654.22 | 430.75 | 861 | 603 |
| Ion optics chamber | 1414 | 448 | 526 | 540.52 | 296.12 | 875 | 662 |
| QMS chamber | 6336 | 2006 | 2355 | 531.36 | 406.61 | 580 | 510 |

Table 3: Conductance of connections via which the chambers are pumped and the effective and normal pumping speed in each chamber for helium and argon.

## 4.5 Pressure gauges

Different pressure gauges have been used to measure the pressure in each chamber and the gas cell. Some gauges do not have a gas dependency, and thus give the pressure value within the chamber directly. Other gauges are gas dependent, and have correction factors for each gas type which need to be applied to the pressure reading as follows:

$$P_{tot} = (P_m - P_b)F + P_b, \tag{20}$$

where $P_{tot}$ denotes the actual pressure within the chamber, $P_m$ the pressure reading, $P_b$ the base pressure (air) measured before introducing the buffer gas, and $F$ the correction factor.

The pressure gauges used for each chamber, with their correction factors for helium and argon and accuracies, are listed in table 4. The gas cell pressure $P_{gc}$ is measured with a capacitance diaphragm gauge, Inficon CDG025D, which is gas independent. The gas cell chamber pressure

$P_1$ and the middle chamber pressure $P_2$ are measured with a pirani gauge, TPR 010, in the range $10^{-3} - 10^{3}$ mbar, and with a cold cathode gauge, IKR 050, in the range $10^{-9} - 10^{-3}$ mbar. Both are gas dependent. The QMS chamber pressure $P_3$ is measured with an ATMION wide range gauge, combining a heat loss sensor based on the Pirani principle with a Bayard-Alpert ion gauge.

| Chamber | Pressure gauge | Accuracy | Correction factor | |
|---|---|---|---|---|
| | | | He | Ar |
| Gas cell chamber $P_{gc}$ | Inficon CDG025D | ±0.20% of reading | none | none |
| Gas cell chamber $P_1$ and Middle chamber $P_2$ | TRP 010 | ±20% | 5.9 | 0.8 |
| | IKR 050 | ±30% | 5.9 | 0.8 |
| QMS chamber $P_3$ | ATMION | ±10% | 5.0 | 0.7 |

Table 4: Accuracy and correction factors of the pressure gauges used [14–17].

# 5 Pressure measurements

The pressure range of the gas cell is restricted by the operational pressure of the QMS chamber because it holds an EMT detector, whose operation requires a chamber pressure of $<10^{-5}$ mbar. Thus, in order to know the operational gas cell pressure range, the behavior of the chamber pressure with respect to gas cell pressure was investigated and will be presented in this section.

## 5.1 Base pressure

After all connections were made between the chambers and pumps and electric feedthroughs, the chambers were pumped down to vacuum.

The air leak rate (in the middle and QMS chamber) was estimated by measuring how fast the pressure dropped after the pumps were turned off. This was done by pumping each chamber to its baseline pressure, turning off the pumps and then measuring the pressure over time until it reached a stable value. The obtained results were plotted and are shown in figure 13. The sudden pressure drop seen at $t = 500$ s originated when changing from the pirani to penning gauge. A linear fit was applied to

the data, whose slope gives the rate of pressure loss. The total volume of the middle and QMS chamber was estimated to be $V_{tot} \approx 7.7$ l. This estimation was calculated using Autodesk Inventor software where the dimensions of each chamber can be found.

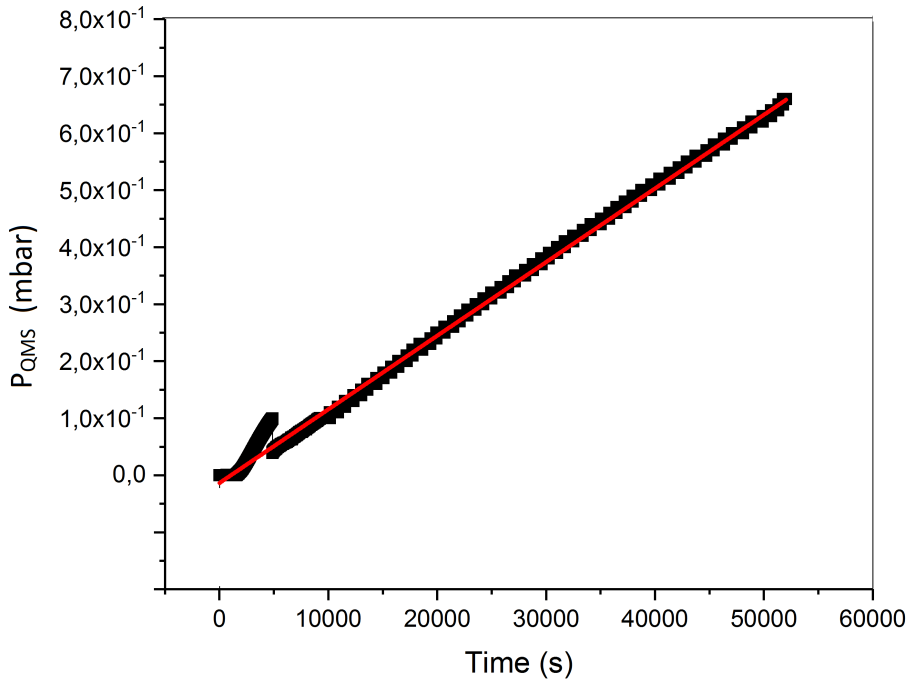


Figure 13: QMS chamber pressure as a function of time.

The combined rate of air leak, outgassing and permeation can then be estimated as follows [10]

$$Q = \frac{d(PV)}{dt} = V \cdot \frac{dP}{dt}. \tag{21}$$

Using the equation above, the air leak rate was calculated to be $Q = 1.025 \cdot 10^{-4}$ mbar.l.s$^{-1}$. The rate is quite high and indicates possible leaks in the chambers.

Before any measurements, a leak detection was therefore conducted using a helium leak detector, Varian PD03 V5, in order to search for and fix any leaks. The leak detector consists of a magnetic sector mass spectrometer and includes a vacuum system to achieve the operational pressure for mass analysis. The tracer gas (helium) that leaks into the cham-

ber is ionized in vacuum. The ions are accelerated and then separated by the magnetic fields (into the analyzer cell), and its current transformed into electric current. The current measured is directly proportional to the helium concentration and thus to the leak value.

From the different existing detection methods, we used the local detection with vacuum method, where helium gas is sprayed to the outer surface of the chamber with a spray gun. Helium is considered to be the best option as a tracer gas because it is an inert, non flammable and non-toxic gas, has low atomic mass that allows penetration through very small leaks and good separation in a mass spectrometer.

Some leaks were found in a number of flange connections that needed tightening. The biggest leak however was found in the gate valve between the gas cell and middle chamber and was thus replaced with a new one.

The ultimate base pressure of a vacuum system is restricted by the gas load, which includes outgassing, leaks and permeation from materials of the wall and o-rings. The base pressure $P_b$ in each chamber can be estimated by dividing the gas load $Q_{load}$ by the effective pumping speed of the vacuum pumps $S_{eff}$:

$$P_b = \frac{Q_{load}}{S_{eff}}, \tag{22}$$

where the effective pumping speed in each chamber has been previously calculated and listed in table 3.

In the estimation, only outgassing from the inner surface of the chambers, using the area of the metal surface exposed to vacuum $A$, and the outgassing rate of the chamber material $q_{outgassing}$, was taken into account as follows:

$$Q_{load} = A \cdot q_{outgassing}. \tag{23}$$

The material of the chambers is stainless steel, and its outgassing rate is estimated to be in the range of $(10^{-9} - 10^{-10})$ mbar.l.s$^{-1}$.cm$^{-2}$ for baked stainless steel and $(10^{-7} - 10^{-9})$ mbar.l.s$^{-1}$.cm$^{-2}$ for unbaked stainless steel [18]. A value of $q_{out.st} = 2333 \cdot 10^{-7}$ W.m$^{-2}$ = $2.333 \cdot 10^{-7}$ mbar.l.s$^{-1}$.cm$^{-2}$ for unbaked stainless steel was used (appendix C.2 [18].)

Table 5 lists the calculated and measured base pressures, without any buffer gas (air). The achieved pressure in the gas cell chamber is two orders of magnitude higher than estimated because it is restricted by the compression ratio of the roots pump, discussed in section 4.3, fig. 11. The measured QMS chamber pressure is about two orders of magnitude lower

than estimated. This can be explained with the choice of the outgassing rate for unbaked stainless steel in the estimation. The longer the chamber is pumped, the more water molecules are removed from the inner walls of the chamber. This case is similar to baking the chamber, during which water molecules are vaporized and pumped away. If using a value of outgassing rate for baked stainless steel in the estimation, the pressure value becomes two order of magnitude lower, and thus agrees more with the measured pressure.

| | Surface area $cm^2$ | Estimated pressure mbar | Measured pressure mbar |
|---|---|---|---|
| Gas cell chamber | 12000 | $9.44 \cdot 10^{-6}$ | $8.3 \cdot 10^{-4}$ |
| Middle chamber | 2150 | $2.42 \cdot 10^{-6}$ | $5.8 \cdot 10^{-6}$ |
| QMS chamber | 3000 | $3.61 \cdot 10^{-6}$ | $6.3 \cdot 10^{-8}$ |

Table 5: Estimated and measured chamber base pressures.

## 5.2 Chamber pressure behavior with respect to gas cell pressure

In this section a study of the behavior of the chamber pressures as a function of gas cell pressure using helium and argon will be presented. Different exit hole (nozzle) diameters and different distances between the exit hole and the skimmer electrode have been tested. A theoretical study is presented first, followed by the experimental study.

The first measurements were conducted without the skimmer and using an exit hole diameter of $d_{nozzle} = 1.2$ mm only. The rest of the measurements were conducted with the skimmer and three different exit hole diameters $d_{nozzle} = 1.2$ mm, 0.9 mm and 0.5 mm.

### 5.2.1 Theoretical study

The pressure in each chamber with respect to the gas cell pressure ($P_0$) was calculated using the conductances between each chamber $C_{1-2}$ and $C_{2-3}$, eq. 11, the throughput of the buffer gas through the exit hole, eq. 6, and the pumping speed. The pressure in the gas cell chamber $P_1$, housing

the gas cell, was determined by

$$P_1 = \frac{Q}{S_{eff}},$$

whereas in the middle chamber, $P_2$, and the QMS chamber, $P_3$, using eq. 4 and 5

$$P_2 = P_1 \frac{C_{1-2}}{C_{1-2} + S_{eff}}, \tag{24}$$

$$P_3 = P_2 \frac{C_{2-3}}{C_{2-3} + S_{eff}}. \tag{25}$$

Table 6 shows a sample of the calculated values for helium as buffer gas, in the case without skimmer $D_{1-2} = 3.9$ mm, and with an exit hole of $d_{nozzle} = 1.2$ mm. In comparison, table 7 shows values with the skimmer electrode $D_{1-2} = 1.03$ mm.

| $P_0$ | $P_1$ | $P_2$ | $P_3$ |
|---|---|---|---|
| 8 | 7.93E-03 | 5.48E-05 | 3.44E-06 |
| 20 | 1.98E-02 | 1.37E-04 | 8.60E-06 |
| 50 | 4.95E-02 | 3.42E-04 | 2.15E-05 |
| 100 | 9.91E-02 | 6.85E-04 | 4.30E-05 |
| 150 | 1.49E-01 | 1.03E-03 | 6.45E-05 |
| 200 | 1.98E-01 | 1.37E-03 | 8.60E-05 |
| 300 | 2.97E-01 | 2.05E-03 | 1.29E-04 |
| 400 | 3.96E-01 | 2.74E-03 | 1.72E-04 |

Table 6: Calculated chamber pressures without skimmer for helium, all values are in mbar.

| $P_0$ | $P_1$ | $P_2$ | $P_3$ |
|---|---|---|---|
| 8 | 7.93E-03 | 3.85E-06 | 2.42E-07 |
| 20 | 1.98E-02 | 9.62E-06 | 6.04E-07 |
| 50 | 4.95E-02 | 2.40E-05 | 1.51E-06 |
| 100 | 9.91E-02 | 4.81E-05 | 3.02E-06 |
| 150 | 1.49E-01 | 7.21E-05 | 4.53E-06 |
| 200 | 1.98E-01 | 9.62E-05 | 6.04E-06 |
| 300 | 2.97E-01 | 1.44E-04 | 9.06E-06 |
| 400 | 3.96E-01 | 1.92E-04 | 1.21E-05 |

Table 7: Calculated chamber pressures with skimmer for helium, all values are in mbar.

### 5.2.2 Experimental study

The measurement process consisted of recording pressure readings from each chamber by varying the pressure in the gas cell, using helium and argon as buffer gas. The first measurements were conducted without the skimmer electrode with a gas cell exit hole of $d_{nozzle} = 1.2$ mm only, at 6 distances of the exit hole from the middle chamber. The rest of the measurements were conducted with the skimmer and three different exit hole diameters $d_{nozzle} = 1.2$ mm, 0.9 mm and 0.5 mm, at 5 distances.

The gas cell was positioned such that the exit hole aligns with the aperture connecting to the middle chamber, and the distance between the exit hole and aperture was set as close as possible. After the baseline vacuum was achieved in each chamber, pressure readings were recorded by introducing the buffer gas to the gas cell through the needle valve thus increasing its pressure. The next set of data was collected moving the gas cell 5 mm further from the middle chamber and so on. Table 8 shows a sample of the obtained results at distance $d_2 = 15$ mm, with an exit hole $d_{nozzle} = 1.2$ mm and without the skimmer, aperture $D_{1-2} = 3.9$ mm, for helium.

The subsequent measurements were conducted with the skimmer $D_{1-2} = 1.03$ mm, first with a gas cell exit hole $d_{nozzle} = 1.2$ mm, then with $d_{nozzle} = 0.9$ mm and last with $d_{nozzle} = 0.5$ mm. Tables 9, 10 and 11 show a sample of the results obtained at a distance $d_2 = 15$ mm, with exit holes 1.2mm, 0.9mm and 0.5mm, respectively. The pressure readings $P_i$ were corrected to $P_{i.eff}$ using eq. 20 with the correction factors listed in table 4.

| $P_0$ | $P_{0error}$ | $P_1$ | $P_{1eff}$ | $P_{1error}$ | $P_2$ | $P_{2eff}$ | $P_{2error}$ | $P_3$ | $P_{3eff}$ | $P_{3error}$ |
|---|---|---|---|---|---|---|---|---|---|---|
| 8.1 | 0.16 | 8.00E-04 | 8.00E-04 | 2.40E-04 | 3.30E-05 | 1.88E-04 | 9.90E-06 | 7.92E-07 | 3.58E-06 | 7.92E-08 |
| 16.1 | 0.32 | 1.70E-03 | 6.11E-03 | 5.10E-04 | 7.50E-05 | 4.36E-04 | 2.25E-05 | 1.19E-06 | 5.57E-06 | 1.19E-07 |
| 24 | 0.48 | 3.00E-03 | 1.38E-02 | 9,00E-04 | 1.20E-04 | 7.01E-04 | 3-60E-05 | 1.60E-06 | 7.62E-06 | 1.60E-07 |
| 32.4 | 0.65 | 4.50E-03 | 2.26E-02 | 1.35E-03 | 4.10E-04 | 2.41E-03 | 1.23E-04 | 3.68E-06 | 1.80E-05 | 3.68E-07 |
| 41.2 | 0.82 | 6.10E-03 | 3.21E-02 | 1.83E-03 | 1.80E-03 | 1.06E-02 | 5.40E-04 | 5.40E-05 | 2.69E-04 | 5.40E-06 |
| 48.6 | 0.97 | 2.70E-02 | 0.155 | 8.10E-03 | 3.70E-03 | 2.18E-02 | 1.11E-03 | 1.44E-04 | 7.19E-04 | 1.44E-05 |
| 52.4 | 1.05 | 2.90E-02 | 0.167 | 8.70E-03 | 4.90E-03 | 2.89E-02 | 1.47E-03 | 2.02E-04 | 1.01E-04 | 2.02E-05 |

Table 8: Measured chamber pressures without skimmer and gas cell exit hole diameter $d_{nozzle} = 1.2$ mm for helium. All values are in mbar. Uncertainties on each pressure measurement are provided using the accuracy of the different gauges as detailed in table 4.

| $P_0$ | $P_{0error}$ | $P_1$ | $P_{1eff}$ | $P_{1error}$ | $P_2$ | $P_{2eff}$ | $P_{2error}$ | $P_3$ | $P_{3eff}$ | $P_{3error}$ |
|---|---|---|---|---|---|---|---|---|---|---|
| 8.1 | 0.016 | 8.30E-04 | 8.79E-04 | 2.49E-04 | 1.70E-05 | 6.16E-05 | 5.10E-06 | 3.92E-07 | 1.61E-06 | 3.92E-08 |
| 19.9 | 0.039 | 2.60E-03 | 1.13E-02 | 7.80E-04 | 1.80E-05 | 6.75E-05 | 5.40E-06 | 4.23E-07 | 1.77E-06 | 4.23E-08 |
| 49.9 | 0.099 | 2.90E-03 | 1.31E-02 | 8.70E-04 | 2.90E-05 | 1.32E-04 | 8.70E-06 | 5.88E-07 | 2.59E-06 | 5.88E-08 |
| 90.2 | 0.18 | 5.40E-02 | 3.15E-01 | 1.62E-02 | 4.40E-05 | 2.21E-04 | 1.32E-05 | 8.24E-07 | 3.77E-06 | 8.24E-08 |
| 148.1 | 0.30 | 9.70E-02 | 5.68E-01 | 2.91E-02 | 7.00E-05 | 3.74E-04 | 2.10E-05 | 1.19E-06 | 5.60E-06 | 1.19E-07 |
| 199.3 | 0.39 | 1.40E-01 | 8.22E-01 | 4.20E-02 | 9.50E-05 | 5.22E-04 | 2.85E-05 | 1.51E-06 | 7.20E-06 | 1.51E-07 |
| 300.5 | 0.60 | 2.00E-01 | 1.18 | 6.00E-02 | 1.30E-04 | 7.28E-04 | 3.90E-05 | 2.12E-06 | 1.03E-05 | 2.12E-07 |
| 349.5 | 0.70 | 2.30E-01 | 1.35 | 6.90E-02 | 1.40E-04 | 7.87E-04 | 4.20E-05 | 2.34E-06 | 1.14E-05 | 2.34E-07 |
| 399.6 | 0.80 | 2.70E-01 | 1.59 | 8.10E-02 | 1.70E-04 | 9.64E-04 | 5.10E-05 | 2.75E-06 | 1.34E-05 | 2.75E-07 |
| 500.6 | 1.001 | 3.40E-01 | 2.00 | 1.02E-01 | 5.20E-04 | 3.03E-03 | 1.56E-04 | 7.51E-06 | 3.72E-05 | 7.51E-07 |
| 599.7 | 1.20 | 4.20E-01 | 2.47 | 1.26E-01 | 1.60E-03 | 9.40E-03 | 4.80E-04 | 3.52E-05 | 1.76E-04 | 3.52E-06 |
| 694.5 | 1.39 | 5.10E-01 | 3.00 | 1.53E-01 | 4.40E-03 | 2.59E-02 | 1.32E-03 | 8.59E-05 | 4.29E-04 | 8.59E-06 |
| 800.3 | 1.60 | 6.10E-01 | 3.59 | 1.83E-01 |  | - | - | 2.59E-04 | 1.29E-03 | 2.59E-05 |
| 897.7 | 1.80 | 7.10E-01 | 4.18 | 2.13E-01 | 1.10E-02 | 6.49E-02 | 3.30E-03 | 9.50E-04 | 4.75E-03 | 9.50E-05 |

Table 9: Measured chamber pressures with skimmer and gas cell exit hole diameter $d_{nozzle} = 1.2$ mm, for helium. All values are in mbar.

| $P_0$ | $P_{0error}$ | $P_1$ | $P_{1eff}$ | $P_{1error}$ | $P_2$ | $P_{2eff}$ | $P_{2error}$ | $P_3$ | $P_{3eff}$ | $P_{3error}$ |
|---|---|---|---|---|---|---|---|---|---|---|
| 3 | 0.006 | 7.35E-04 | 4.66E-04 | 2.21E-04 | 1.50E-05 | 1.01E-05 | 4.50E-06 | 2.45E-07 | 6.05E-07 | 2.45E-08 |
| 13.5 | 0.027 | 9.50E-04 | 1.73E-03 | 2.85E-04 | 1.60E-05 | 1.60E-05 | 4.80E-06 | 2.53E-07 | 6.45E-07 | 2.53E-08 |
| 50.7 | 0.10 | 3.70E-03 | 1.80E-02 | 1.11E-03 | 2.00E-05 | 3.96E-05 | 6.00E-06 | 3.06E-07 | 9.10E-07 | 3.06E-08 |
| 99.6 | 0.19 | 2.60E-02 | 1.50E-01 | 7.80E-03 | 2.90E-05 | 9.27E-05 | 8.70E-06 | 4.00E-07 | 1.38E-06 | 4.00E-08 |
| 149.9 | 0.29 | 3.90E-02 | 2.26E-01 | 1.17E-02 | 3.70E-05 | 1.40E-04 | 1.11E-05 | 5.05E-07 | 1.91E-06 | 5.05E-08 |
| 200.7 | 0.40 | 5.10E-02 | 2.97E-01 | 1.53E-02 | 4.85E-05 | 2.08E-04 | 1.46E-05 | 6.03E-07 | 2.39E-06 | 6.03E-08 |
| 299.7 | 0.59 | 7.80E-02 | 4.56E-01 | 2.34E-02 | 7.10E-05 | 3.41E-04 | 2.13E-05 | 7.92E-07 | 3.34E-06 | 7.92E-08 |
| 400.9 | 0.80 | 1.10E-01 | 6.45E-01 | 3.30E-02 | 9.00E-05 | 4.53E-04 | 2.70E-05 | 9.22E-07 | 3.99E-06 | 9.22E-08 |
| 499.3 | 0.99 | 1.40E-01 | 8.22E-01 | 4.20E-02 | 1.00E-04 | 5.12E-04 | 3.00E-05 | 1.06E-06 | 4.68E-06 | 1.06E-07 |
| 546.9 | 1.09 | 1.60E-01 | 9.40E-01 | 4.80E-02 | 1.00E-04 | 5.12E-04 | 3.00E-05 | 1.11E-06 | 4.93E-06 | 1.11E-07 |
| 599.6 | 1.20 | 1.70E-01 | 9.99E-01 | 5.10E-02 | 1.10E-04 | 5.71E-04 | 3.30E-05 | 1.17E-06 | 5.23E-06 | 1.17E-07 |
| 700.2 | 1.40 | 1.90E-01 | 1.12E+00 | 5.70E-02 | 1.20E-04 | 6.30E-04 | 3.60E-05 | 1.36E-06 | 6.18E-06 | 1.36E-07 |

Table 10: Measured chamber pressures with skimmer and gas cell exit hole diameter $d_{nozzle} = 0.9$ mm, for helium. All values are in mbar.

| $P_0$ | $P_{0error}$ | $P_1$ | $P_{1eff}$ | $P_{1error}$ | $P_2$ | $P_{2eff}$ | $P_{2error}$ | $P_3$ | $P_{3eff}$ | $P_{3error}$ |
|---|---|---|---|---|---|---|---|---|---|---|
| 28.5 | 0.057 | 1.00E-03 | 1.88E-03 | 3.00E-04 | 3.50E-06 | 7.00E-08 | 1.05E-06 | 1.04E-07 | 2.74E-07 | 1.04E-08 |
| 50 | 0.10 | 3.85E-03 | 1.87E-02 | 1.16E-03 | 4.80E-06 | 7.74E-06 | 1.44E-06 | 1.19E-07 | 3.49E-07 | 1.19E-08 |
| 99.7 | 0.20 | 1.20E-02 | 6.68E-02 | 3.60E-03 | 8.70E-06 | 3.08E-05 | 2.61E-06 | 1.59E-07 | 5.49E-07 | 1.59E-08 |
| 150 | 0.30 | 2.00E-02 | 1.14E-01 | 6.00E-03 | 1.20E-05 | 5.02E-05 | 3.60E-06 | 2.05E-07 | 7.79E-07 | 2.05E-08 |
| 200.4 | 0.40 | 2.50E-02 | 1.43E-01 | 7.50E-03 | 1.45E-02 | 8.55E-02 | 4.35E-03 | 2.54E-07 | 1.02E-06 | 2.54E-08 |
| 300.6 | 0.60 | 3.70E-02 | 2.14E-01 | 1.11E-02 | 2.20E-05 | 1.09E-04 | 6.60E-06 | 3.56E-07 | 1.53E-06 | 3.56E-08 |
| 399.7 | 0.80 | 4.90E-02 | 2.85E-01 | 1.47E-02 | 3.00E-05 | 1.56E-04 | 9.00E-06 | 4.72E-07 | 2.11E-06 | 4.72E-08 |
| 500.5 | 1.00 | 6.20E-02 | 3.62E-01 | 1.86E-02 | 3.70E-05 | 1.98E-04 | 1.11E-05 | 5.47E-07 | 2.49E-06 | 5.47E-08 |
| 600.4 | 1.20 | 7.60E-02 | 4.44E-01 | 2.28E-02 | 4.50E-05 | 2.45E-04 | 1.35E-05 | 6.72E-07 | 3.11E-06 | 6.72E-08 |
| 699.2 | 1.39 | 9.20E-02 | 5.39E-01 | 2.76E-02 | 5.30E-05 | 2.92E-04 | 1.59E-05 | 7.48E-07 | 3.49E-06 | 7.48E-08 |

Table 11: Measured chamber pressures with skimmer and gas cell exit hole diameter $d_{nozzle} = 0.5$ mm, for helium. All values are in mbar.

The results of each measurement were plotted and can be found in appendices A and B. The plot in figure 14 shows the measured chamber pressures for helium and argon with nozzle size $d_{nozzle} = 0.9$ mm as a function of gas cell pressure. Lower pressures are achieved with argon in the gas cell chamber and QMS chamber compared to helium, which is explained by the higher conductance values with helium.

Figure 15 shows a comparison of the measured and theoretical results for helium with nozzle size $d_{nozzle} = 0.9$ mm. A quite good concordance between the results can be seen.

Figure 16 illustrates the measured pressures for helium with and without the skimmer system. Lower pressures in each chamber are achieved with the skimmer system at higher gas cell pressures. This is due to the aperture diameter, being three times larger than the skimmer diameter, which leads to a higher conductance and thus higher pressures in the chambers. Without the skimmer system, a sudden increase in the pressures is seen after $P_{gc} = 40$ mbar and the gas cell pressure couldn't be raised more than 80 mbar without exceeding the operational pressure in the QMS chamber. Yet, the reason for this pressure behavior is unknown.

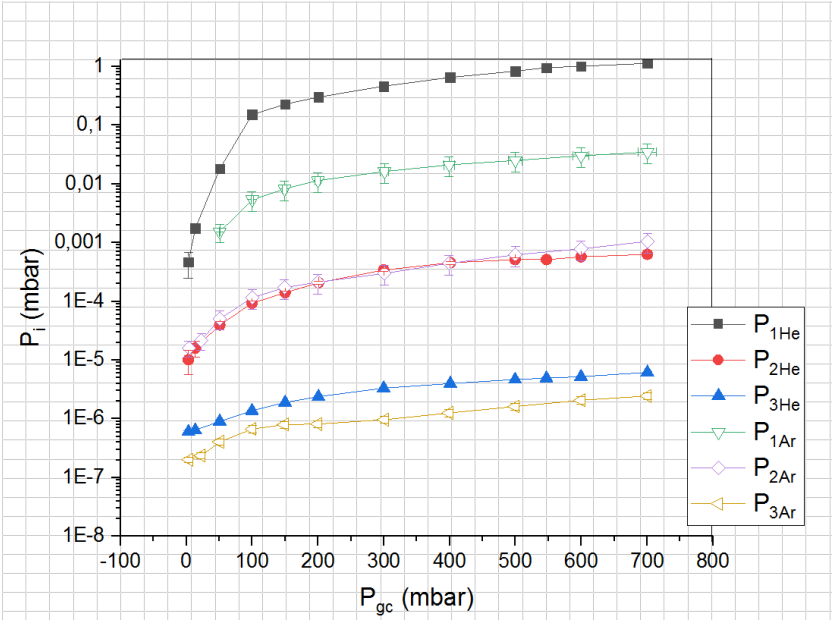


Figure 14: Measured chamber pressures as function of gas cell pressure with nozzle $d_{nozzle} = 0.9$ mm for helium ($P_{iHe}$) and argon ($P_{iAr}$).

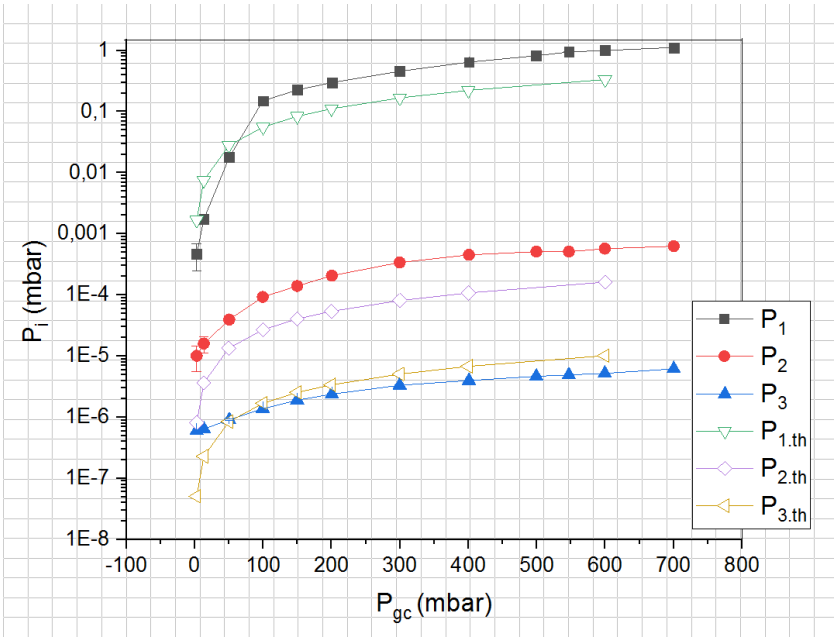


Figure 15: Measured ($P_i$) and theoretical ($P_{i.th}$) chamber pressures as a function of gas cell pressure ($P_{gc}$) with gas cell nozzle diameter $d_{nozzle} = 0.9$ mm, for helium.

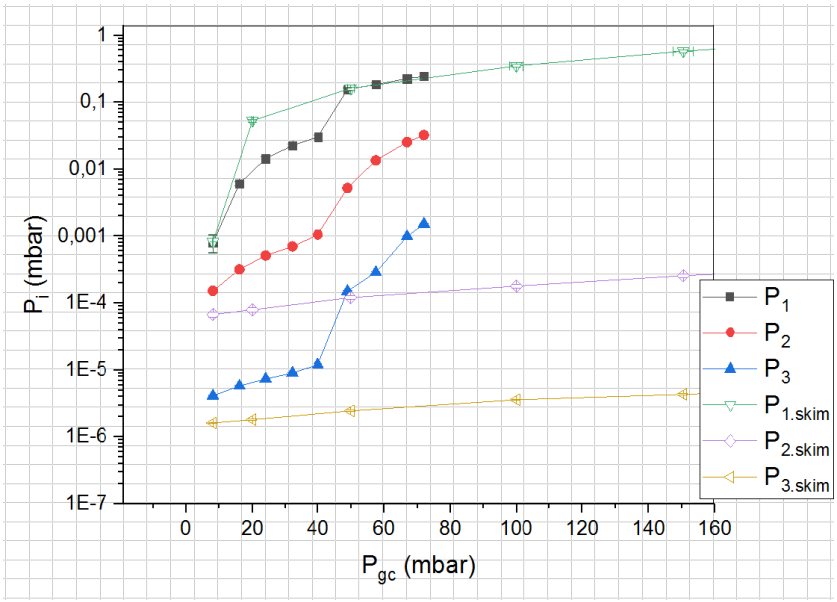


Figure 16: Measured chamber pressures as function of gas cell pressure with ($P_{i.skim}$) and without ($P_i$) the skimmer electrode, for helium.

To look at the behavior of the chamber pressures with respect to the gas cell pressure at different exit holes/nozzle sizes, the results obtained for helium at a distance $d_2 = 15$ mm from the middle chamber with the skimmer were used. Figure 17 shows the measured chamber pressures as a function of nozzle size at a gas cell pressure $P_{gc} = 100$ mbar, as well as the theoretical values. The smaller the exit hole the lower the pressure in each chamber and a good agreement between the theoretical and measured pressures can be seen.

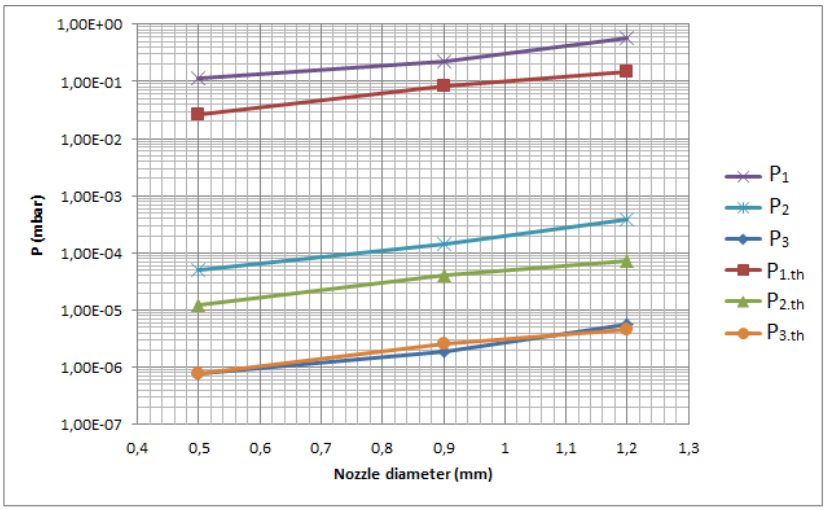


Figure 17: Experimental ($P_i$) and theoretical ($P_{i.th}$) chamber pressures with 3 different exit hole diameters at gas cell pressure $P_{gc} = 100$ mbar, for helium.

In addition, we can look at the behavior of the chamber pressures at different distances of the gas cell from the middle chamber. For this, the obtained results in the case of helium with an exit hole diameter $d_{nozzle} = 0.9$ mm and the skimmer electrode were used. Figure 18 shows the pressures in the middle and QMS chamber as a function of distance at gas cell pressure $P_{gc} = 150$ mbar and gas cell chamber pressure $P_1 = 0.11$ mbar. There is a steady decrease in both chamber pressures as the distance between the gas cell and middle chamber increases.

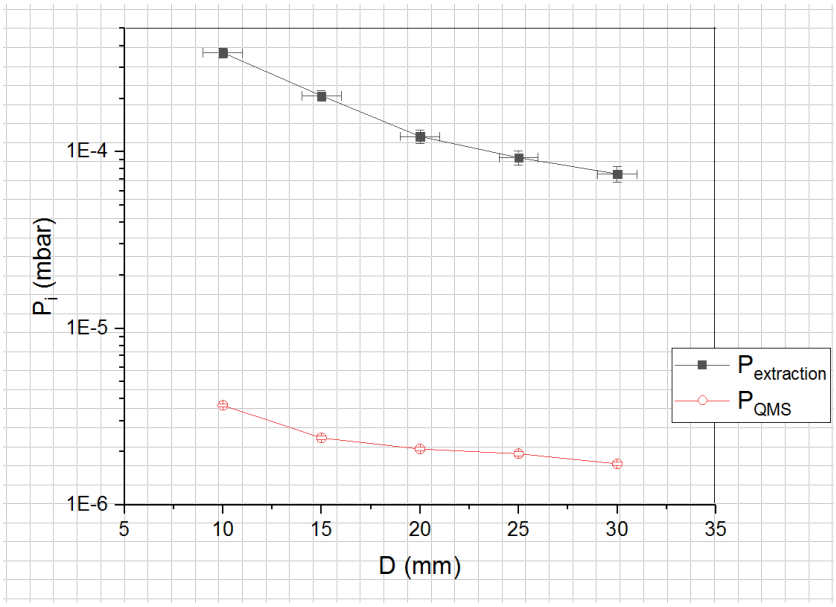


Figure 18: Chamber pressures ($P_i$) as a function of gas cell position $D$ (distance from middle chamber) at gas cell pressure $P_{gc} = 150$ mbar and gas cell chamber pressure $P_1 = 0.11$ mbar.

## 5.3 Summary

The measured chamber pressures are in good agreement with the calculated values, as illustrated in the example given in figure 15, for all the measurements conducted with helium and argon. The achieved pressures are lower for argon compared to helium (fig.14), which is expected since the conductance is higher for helium.

The experiments proved the advantage of using the skimmer system in order to achieve lower pressures in the chambers therefore enabling the use of higher gas cell pressures for future experiments as shown in figure 16. Furthermore, slightly lower pressures were achieved using smaller exit holes as estimated, as can be seen in figure 17, and a good agreement was achieved with calculations.

There is a slight drop in the second chamber and QMS chamber pressure as the gas cell is moved further from the skimmer electrode, fig. 18.

# 6 Performance of the ion guide system and transport efficiency

The performance and efficiency of an ion guide/gas cell can be tested using long-lived radioactive alpha recoil sources. As has been previously done several times at the IGISOL–facility [19], a radioactive $^{223}$Ra $\alpha$-recoil source was used to investigate the transmission efficiency of the ion guide system.

The $^{223}$Ra $\alpha$-recoil source was generated in-house from $^{227}$Ac which has a half-life of 21.8 years. The granddaughter $^{223}$Ra atoms are implanted on the top of a metal needle that is mounted within the gas cell. Figure 19 shows the decay chain for $^{223}$Ra ($T_{1/2}$=11.4 d). $^{223}$Ra alpha decays into $^{219}$Rn, half of which recoils out of the source into the gas cell and is thermalized in the helium gas. The other half recoils into the source and is therefore unavailable for the measurement. The thermalized daughter products are guided to the exit hole in a helium flow, and further towards a silicon detector where they are implanted and the alpha decay is recorded. The $^{219}$Rn recoils are emitted as ions with an energy of 100 keV and have an average stopping range of 5 mm in 100 mbar room temperature helium gas. They are therefore easily stopped in the helium gas. The half-lives of $^{223}$Ra ($T_{1/2}$=11.4 d), $^{219}$Rn ($T_{1/2}$=4 s), and $^{215}$Po ($T_{1/2}$=1.8 ms), compared to the evacuation time of the gas cells, make them ideal nuclei for probing the efficiency of gas cells and ion transport systems, and the alpha decay allows easy detection of these nuclei.

During the transport, radioactive decay losses occur. However these can be neglected since the half-life of $^{219}$Rn is longer than the transport time through the gas cell.

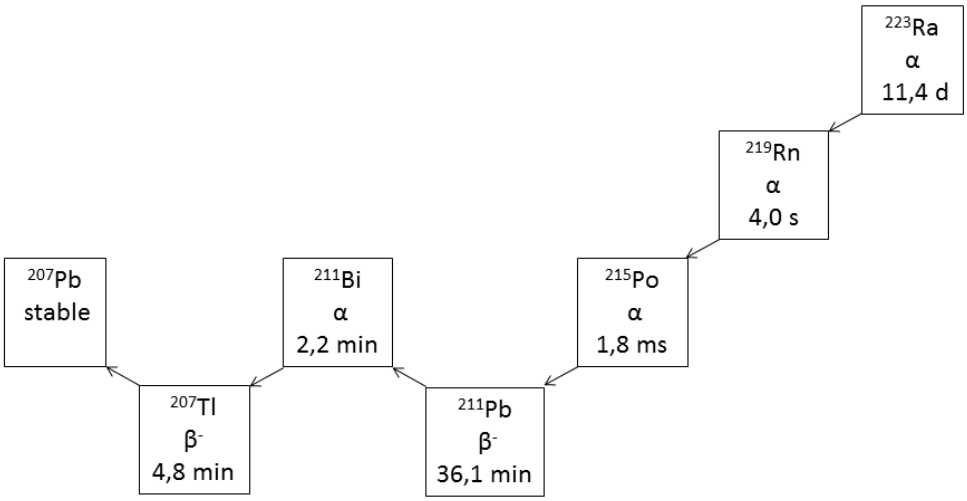


Figure 19: The $^{223}$Ra decay chain.

The total efficiency is calculated from the ratio of the particle activities [20]:

$$\epsilon = \frac{A(^{219}\mathrm{Rn})}{A(^{223}\mathrm{Ra})}. \tag{26}$$

The activity of the source $A_s(^{223}\mathrm{Ra})$, in turn, can be calculated from the measured $\alpha$-counts N($^{223}$Ra), the branching ratio of the $\alpha$-channel b.r($^{223}$Ra), the solid angle of the source to detector $\Omega$ and the measurement time $T$ as follows:

$$A(^{223}\mathrm{Ra}) = \frac{N(^{223}\mathrm{Ra})}{b.r(^{223}\mathrm{Ra}) \times \Omega \times T}. \tag{27}$$

Similarly, the activity of $A(^{219}\mathrm{Rn})$ can be calculated using the same equation (27), using the silicon detector acceptance instead of solid angle.

## 6.1 Instrumentation

The data acquisition was conducted using a compact desktop system DT5780 Dual Digital MCA, integrating 2 independent 16k channels Digital MCA (digital multi-channel analyzer) [21]. Figure 20 shows a block diagram of the digitizer-based spectroscopy system. The charge sensitive preamplifier converts the collected charge, which is proportional to

the energy deposited in the detector, into a voltage signal. The shaping amplifier provides a quasi-Gaussian output, whose height is proportional to the detected particle energy. The signal is then fed to a peak sensing ADC, which evaluates and digitizes the height of the pulses giving the energy spectrum. The digitizer combines these last two devices, and acts as a digital multi-channel analyzer MCA.

The alpha spectra were recorded using the trapezoidal filter, which, similar to the shaping amplifier, converts the input signal into a trapezoidal signal, whose height is proportional to the energy [21].

Figure 21 shows a schematic of the electronic setup with the traces after each component, recorded with an oscilloscope.

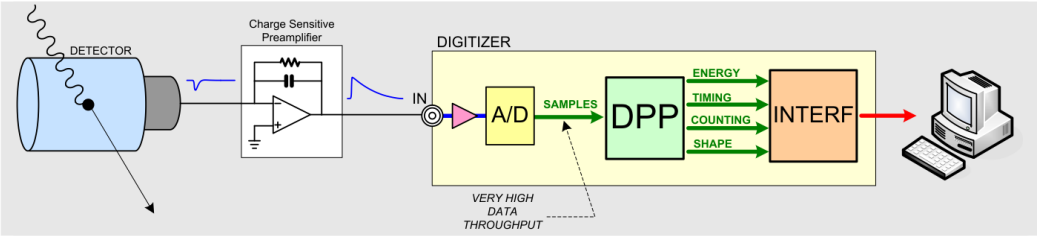


Figure 20: Analog chain block diagram of the DT5780 Dual Digital MCA [21].

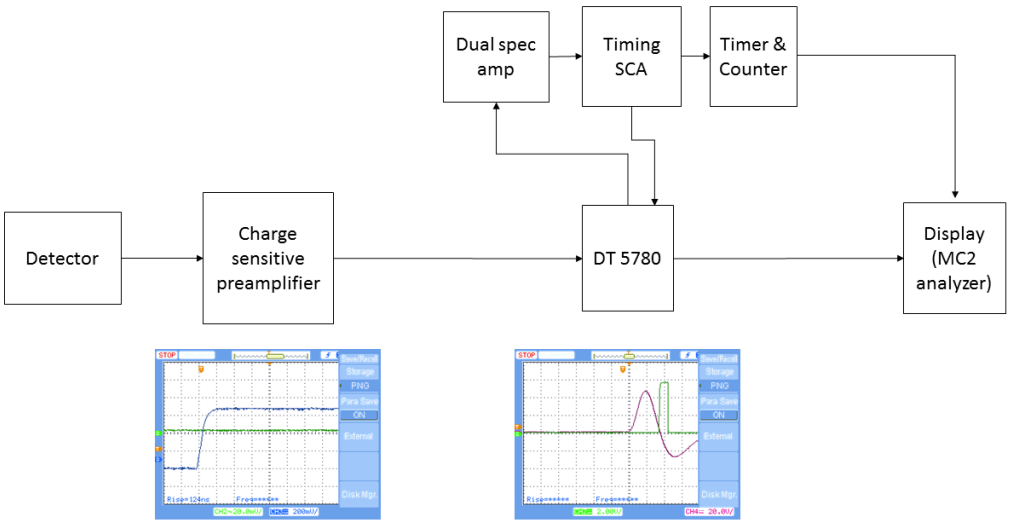


Figure 21: Schematic of the electronic setup with the signal shape recorded with an oscilloscope.

## 6.2 $^{223}$Ra source activity

Before conducting the efficiency measurements, the activity of the source $A(^{223}\text{Ra})$ was measured. This was done under vacuum by removing the nozzle plate from the gas cell and placing a silicon detector directly in front of the gas cell. Data were collected for a duration of $T = 1640$ s. Figure 22 shows the alpha spectrum obtained. The alpha peaks were identified according to their energy and are associated to the different isotopes in the $^{223}$Ra decay chain.

The source was placed at a distance $d = 71.7 \pm 0.5$ mm away from the detector which has a surface area $A_{detector} \approx 380$ mm$^2$, giving a solid angle $\Omega = \frac{A_{detector}}{4\pi d^2} = 5.9 \cdot 10^{-3} \pm 0.5 \cdot 10^{-3}$. The source activity was calculated using eq. 27, with $N(^{223}\text{Ra}) = 10653 \pm 104$ cnts, the $\alpha$ counts from the integral of the peak indicated in figure 22 corresponding to $Ra_2$ of known branching ratio $br = 52.60(13)$ %. This resulted in a value of $A(^{223}\text{Ra}) = (2.10 \pm 0.20)$ kBq.

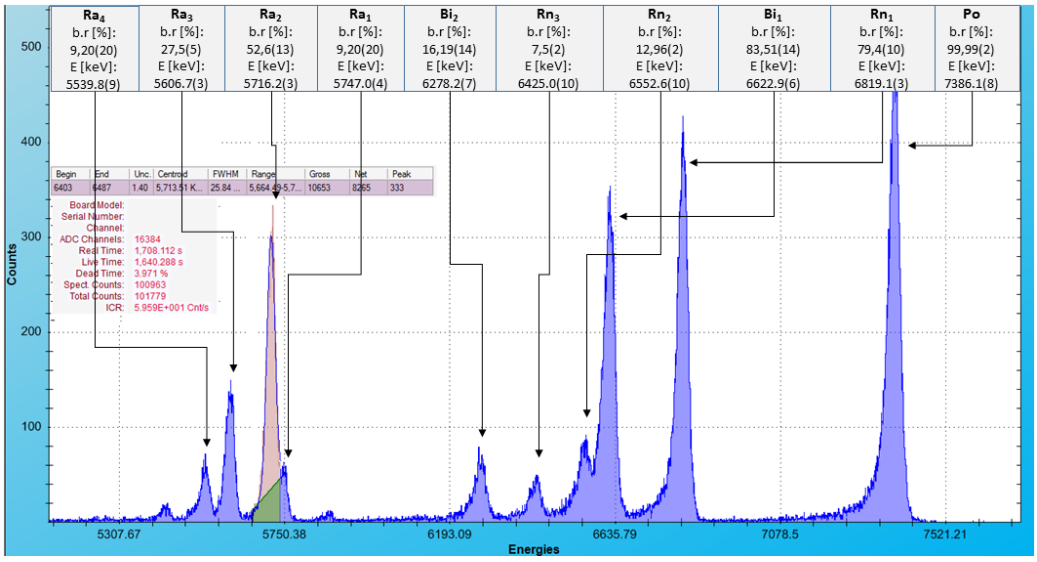


Figure 22: Measured alpha spectrum for determining the source activity $A(^{223}\text{Ra})$. The alpha peaks are labeled according to their respective isotope, and the relevant branching ratios and alpha energies are shown.

The energy calibration of the silicon detector was made using the same spectrum (fig. 22) by associating the channel value to the energy value corresponding to each peak, as shown in figure 23.

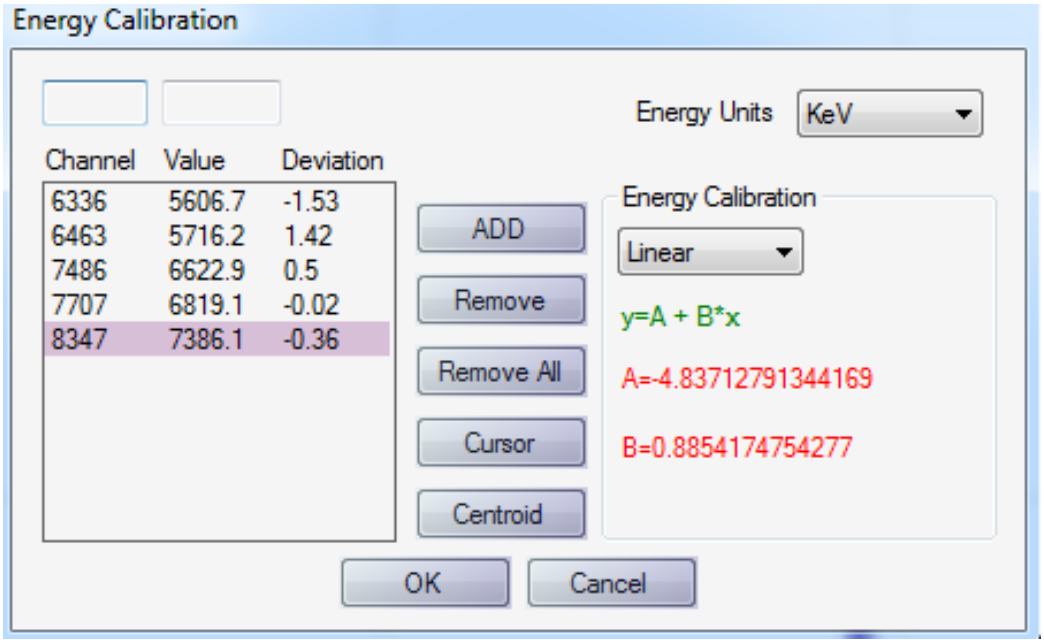


Figure 23: Energy calibration. The channel number is converted to an energy using the alpha decay spectrum of the $^{223}$Ra $\alpha$-recoil source, fig 22.

## 6.3 Gas cell extraction efficiency

In the previous section, the determination of the source activity was described which is done under vacuum without the nozzle plate attached to the gas cell. The next important investigation was to study the extraction efficiency of the gas cell by measuring how many $\alpha$-decay recoils are extracted from the gas cell under operational conditions, though it is not the subject of study.

The Cf gas cell was initially in use, with the source mounted as indicated in figure 3. It was used with a nozzle size $d_{nozzle} = 0.9$ mm, and $\alpha$-decay recoils were collected with the same silicon detector as discussed previously, placed right in front of the gas cell. The gas cell was isolated from the vacuum chamber, thus allowing us to raise its potential to a specific voltage. By applying a voltage of about 200 V on the gas cell, ions are accelerated and implanted directly into the detector.

Unfortunately, we obtained very small yields out of the gas cell and the spectrum illustrated in figure 24 shows the highest $\alpha$ peak for $^{211}$Bi, and only a very small peak for $^{215}$Po and $^{219}$Rn.

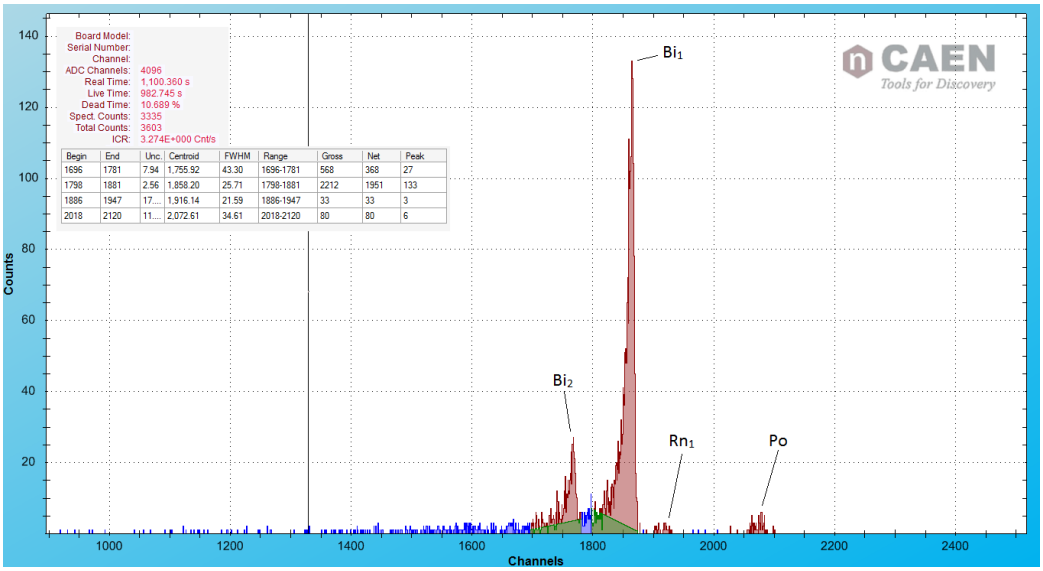


Figure 24: Measured alpha spectrum for determining the source activity $A(^{219}\mathrm{Rn})$, extracted from the Cf gas cell. The data was collected for a duration of 983 s.

A number of attempts were made to improve the yield, first by putting an aluminum foil in front of the detector in order to have the potential of the foil at the same potential as the detector holder, biased to $U_{det.holder} = 50$ V. This was to try to reduce any disturbance to the extracted ion trajectories. No improvements were seen and the foil only added tails to the low-energy side of the alpha peaks and was thus removed. It was then suspected that the windows within the gas cell, being insulators, may have been charged due to the presence of alpha activity. These were covered with aluminum foil but once again, no improvement was seen. Lastly, leaks within the gas cell were suspected, however none were found. Impurities in the gas cell or gas lines are currently thought to be the source for the reduced activity. This hypothesis can only be tested after commissioning the QMS and using the device to obtain a mass spectra.

The Cf gas cell has never been used at the IGISOL–facility, and thus independent studies need to be made in order to have it fully operational. For the time being, the $^{223}$Ra recoil source was transferred to the actinide gas cell (mounted as indicated in figure 4). Because of its smaller volume which translates into a shorter evacuation time, improvement in the ion survival was anticipated.

With the actinide gas cell installed, the signals improved. But still, the overall yield extracted from the gas cell appeared to be low. The gas purification system is still suspected to be the source of the low yield and

will be investigated in the near future.
Since the measurements were conducted $t = 4.083$ days after the source activity $A(^{223}\text{Ra})$ was measured, the half life $T_{1/2} = 11.4$ d of $^{223}$Ra needs to be taken into account as follows

$$A = A_0 2^{-\frac{t}{T_{1/2}}}.$$

Thus the source activity on the measurement day was calculated to be $A(^{223}\text{Ra}) = 1637 \pm 157$ Bq.
The first set of measurements consisted in searching for the optimum extraction pressure of the gas cell after optimizing the voltages of the gas cell and the Si detector holder. The voltage optimization was planned to be performed by measuring alpha spectra at different voltage combinations. Unfortunately, due to lack of time, the optimization of the gas cell voltage and detector holder voltage was simply done by observing the behavior of the count rate when varying the voltages. The highest count rate was observed at a gas cell voltage $U_{gc} = 120$ V and detector holder voltage $U_{det.holder} = 50$ V.

Figure 25 shows the activity of the daughter $^{219}$Rn as a function of helium pressure. The highest activity was obtained at a pressure $P_{gc} = 60$ mbars. At low pressures $^{219}$Rn ions diffuse to the walls of the gas cell where they are neutralized and lost, thus decreasing the activity. At higher pressures the increase in recombination, happening between a singly-charged $^{219}\text{Rn}^+$ ion, an electron and a He atom (thus neutralizing the ion), might be the cause of the decrease in activity. All the measured spectra at different helium pressures can be found in appendix C.

Figure 26 shows the measured spectra at the optimum pressure $P_{gc} = 60$ mbars. Using a silicon detector acceptance of $\Omega = 0.3 \pm 0.05$, branching ratio $b.r(Rn_1) = 79.4(10)\%$, $\alpha$ counts $N(^{219}\text{Rn}) = 897 \pm 30$ cnts and $t = 1061.748$ s, the activity of the daughter nuclei $^{219}$Rn was calculated with eq. 27 to be $A(^{219}\text{Rn}) = 3.55 \pm 0.61$ Bq. The data was collected 6 days after the previous measurements (optimum extraction pressure measurements), explaining the lower activity measured compared to figure 25.

Finally, the efficiency of the gas cell could be determined using eq. 26, (with the source activity $A(^{223}\text{Ra}) = (1070 \pm 103)$ Bq calculated using eq. 6.3, after $t$=7 days from the last activity determination) resulting in $\epsilon = 0.33 \pm 0.07$ %. The extraction efficiency is much lower than expected ($\approx$10 %) and suggests there might be some gas impurity issues which can result in severe recombination losses.

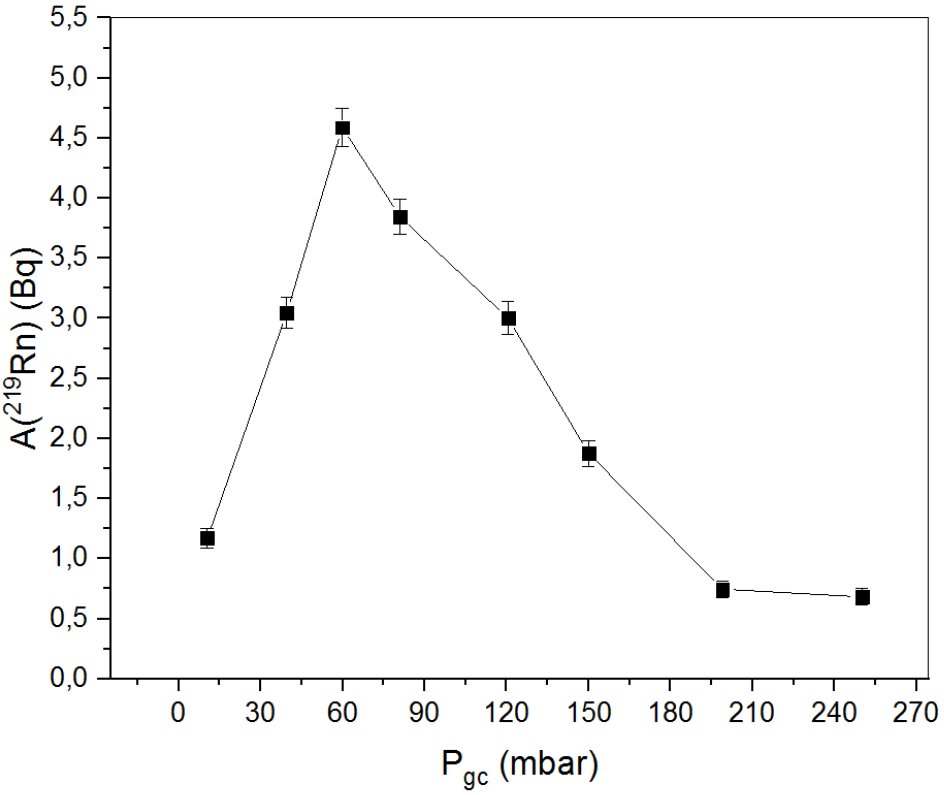


Figure 25: $^{219}$Rn activity as a function of gas cell pressure.

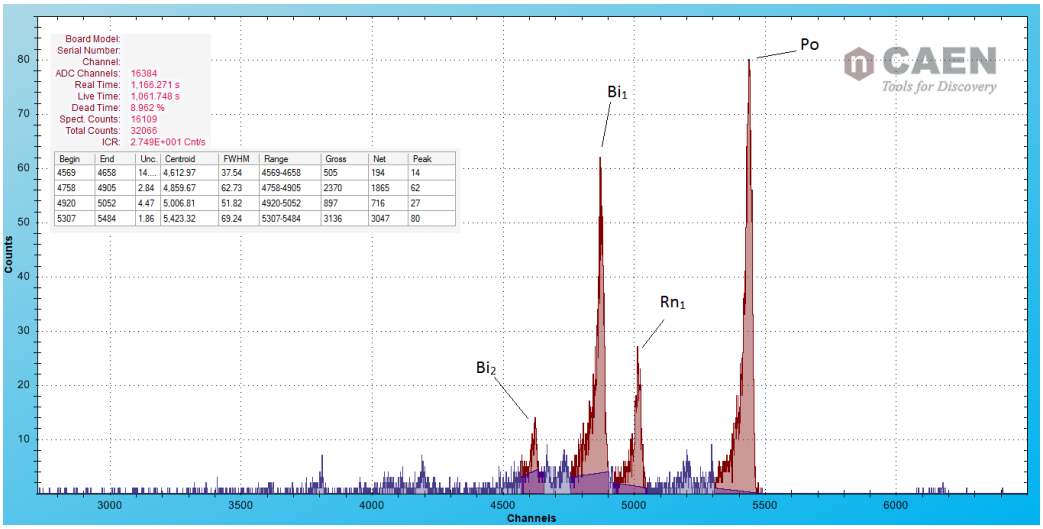


Figure 26: Measured alpha spectrum at an optimum gas cell pressure of 60 mbars.

## 6.4 Squeezer electrode and skimmer transmission efficiency

To study the transmission efficiency of the squeezer-skimmer system, the alpha recoils were transported through the skimmer and recorded by a silicon detector placed just after the gate valve separating the gas cell chamber from the middle chamber (illustrated in the schematic of figure 2). After optimizing the voltages of the gas cell, the squeezer and skimmer system, the spectrum was collected for about 25 min at a gas cell pressure of $P_{gc} = 61.6$ mbars. The obtained spectrum is shown in figure 27.
The optimal voltages were: $U_{gc}$ = 250 V, $U_{squeezer,front}$ = 225 V, $U_{squeezer,mid}$ = 160 V, $U_{squeezer,back}$ = 242 V, $U_{skimmer}$ = 15 V, $U_{extractor}$ = -110 V, $U_{mid,electrode}$ = 107 V and $U_{last,electrode}$ = 0 V.

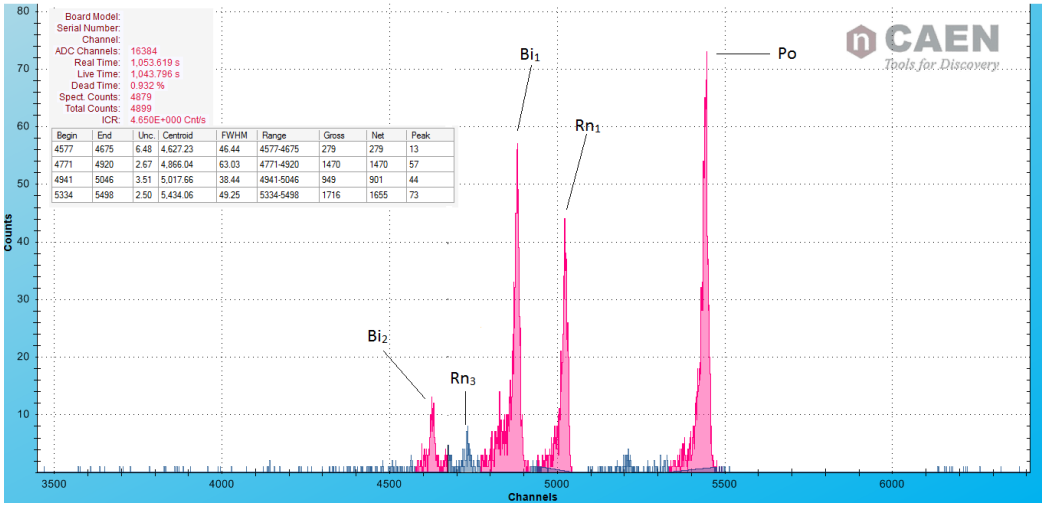


Figure 27: Measured alpha spectrum after the skimmer system.

The activity of the daughter $^{219}$Rn was calculated in a similar manner as the gas cell extraction efficiency determination, using eq. 27, $A(^{219}\text{Rn}) = 3.82 \pm 0.66$ Bq, resulting in a transmission efficiency of $\epsilon_{skimmer} = 108 \pm 26$ %. Efficiency of over 100 % is not possible, and the result obtained is due to the selection of the silicon detector used in the measurements ($\Omega = 0.3 \pm 0.05$). The detector acceptance error is the biggest source of uncertainty.

When comparing the spectra measured before and after the skimmer system, figures 26 and 27, a difference between the relative heights of the $^{219}$Rn and Po peaks is observed. The higher Po peak observed before the skimmer might be due to the direct production of Po from the decay of $^{219}$Rn in the gas cell. The silicon detector (Si1) collects these emitted

alphas in addition to those from the implanted $^{219}$Rn, whereas the silicon detector after the skimmer (Si2) collects only the alphas emitted from Po produced following the implantation of $^{219}$Rn.

## 6.5 Summary

A $^{223}$Ra alpha-recoil source has been used in the first study of the extraction and transport efficiency of the off-line rig. Although the extraction efficiency of the gas cell is not the subject of study, the $\alpha$-spectra obtained with the Cf gas cell showed very little yield for all isotopes, especially for $^{219}$Rn, which indicates a poor efficiency of the gas cell. Further investigation is needed, particularly with regards to the gas purity, before installing any gas cell for future measurements.

Nevertheless, after transferring the source to the actinide gas cell, sufficient alpha decays were detected and the optimum extraction pressure was found to be 60 mbars. At this pressure, the extraction efficiency was calculated to be $\epsilon = 0.33 \pm 0.07$ %. It is very small, and could be a result of gas impurities.

At the optimum extraction pressure and voltages of the gas cell and squeezer-skimmer electrodes, the transmission efficiency of the skimmer system was measured to be $\epsilon_{skimmer} = 108 \pm 26$ %. The over 100 % efficiency obtained is due to the silicon detector acceptance, whose error was the main source of uncertainty. A transmission efficiency of nearly 100 % is ideal for future measurements with the off-line rig.

# 7 Future developments

A $^{223}$Ra $\alpha$-recoil source will be generated again in the near future and installed into the actinide gas cell, or into a small volume light ion guide which has extraction times less than 1 ms. The latter gas cell would be be less affected by possible gas impurities and thus have less efficiency losses. A more careful optimization of voltages of the squeezer-skimmer electrodes and the Einzel lenses of the ion optics can them be made. Following this, the beam will be transported into the QMS chamber and the total transmission efficiency of the whole system can be measured after a full mass analysis.

The off-line rig will be used in the future for the development and testing of a cryogenic ion guide as well as (re)installation of the fission gas cell with a spontaneous $^{252}$Cf fission source. Operating the gas cell at temperatures below 50 K has many advantages. Firstly, the reduction

of impurities in the buffer gas results in improved ion survival, while secondly, the higher density of gas due to reduced temperature improves the stopping efficiency. At the IGISOL–4 facility, the characterization of a cryogenic ion guide has been done in order to improve the production of low-energy beams [22], however due to liquid nitrogen cooling only temperatures close to 100 K were achieved. A new cryocooler was recently purchased and is planned to be coupled via a cold finger to a small volume gas cell and will be mounted within the off-line rig. This will allow a study of the reduction of impurities in the buffer gas as well as the extraction efficiency of radioactive isotopes as a function of temperature from either a $^{223}$Ra $\alpha$-recoil source, or a future spontaneous $^{252}$Cf fission source. An element-dependent study of the extraction efficiency and ion survival can be made with the latter source.

# References


[1] J. Äystö, T. Eronen, A. Jokinen, A. Kankainen, I. Moore, and H. Penttilä. *Three decades of research using IGISOL technique at the University of Jyväskylä*, volume 223. Hyperfine Interactions, 1 edition, 2014.

[2] A. Ivonen, R. Saintola, and K. Valli. Ion-guide quadrupole mass spectrometer. *Physica Scripta*, 42:133–137, 1990.

[3] V.S. Kolhinen, T. Eronen, D. Gorelov, J. Hakala, A. Jokinen, K. Jokiranta, A. Kankainen, M. Koikkalainen, J. Koponen, H. Kulmala, M. Lantz, A. Mattera, I.D. Moore, and H. Penttilä. Recommissioning of jyfltrap at the new igisol-4 facility. *Nuclear Instruments and Methods in Physics Research*, 317:506–509, 2013.

[4] I. D. Moore, P-Dendooven, and J. Ärje. The igisol technique—three decades of developments. *Hyperfine Interactions*, 223:17–62, 2014.

[5] I. Pohjalainen, I.D. Moore, T. Kron, S. Raeder, V. Sonnenschein, H. Tomita, N. Trautmann, A. Voss, and K. Wendt. In-gas-cell laser ionization studies of plutonium isotopes at igisol. *Nuclear Instrumentsand Methods*, 376:233–239, 2016.

[6] I. Pohjalainen, I. D. Moore, T. Eronen, A. Jokinen, H. Penttilä, and S. Rinta-Antila. Gas purification studies at igisol-4. *Hyperfine Interactions*, 227:169–180, 2014.

[7] Paul Wolfgang and Steinwedel Helmut. Notizen: Ein neues massenspektrometer ohne magnetfeld. *Zeitschrift für Naturforschung*, 8:448–450, 1953.

[8] Mikhail Sudakova, Eugenij Mamontova, Fuxing Xub, Chongsheng Xub, and Chuan Fan Dingb. Possibility of operating quadrupole mass filter at high resolution. *International Journal of Mass Spectrometry*, 408:9–19, 2016.

[9] Andrew T. Kicman, Mark C. Parkin, and Ray K. Iles. An introduction to mass spectrometry based proteomics—detection and characterization of gonadotropins and related molecules. *Molecular and Cellular Endocrinology*, 260-262:212–227, 2007.

[10] A. Roth. *Vacuum Technology*. ELSEViER.

[11] *EH Mechanical Booster Pumps Instruction Manual*.

[12] *Diffstak Vapour Diffusion Pumps, Edward product catalogue*.

[13] *EXT Compund Turbomolecular Pumps Instruction Manual*.

[14] *CDG025, Operating manual*.

[15] *Active Wide Range Vacuum Gauge, ATMION Instruction manual*.

[16] *Pirani Gauge TPR 010, BG 805 976 BN, Operating instruction*.

[17] *Cold Cathode Gauge IKR 050, BG 805 031 BE, Operating instruction*.

[18] John F. O'Hanlon. *A User's Guide to Vacuum Technology*. John Wiley & Sons, 3 edition, 2003.

[19] P. Karvonen, I.D. Moore, T. Sonoda, T. Kessler, H. Penttilä, K. Peräjärvi, P. Ronkanen, and J. äystö. A sextupole ion beam guide to improve the efficiency and beam quality at igisol. *Nuclear Instruments and Methods in Physics Research*, 266:4794–4807, 2008.

[20] Reponen Mikael. *Resonance laser ionization developments for IGISOL-4*. PhD thesis, University of Jyväskylä, 2012.

[21] *MC2Analyzer User Manual UM3182, Rev. 4*.

[22] A. Saastamoinen, I.D. Moore, M. Ranjan, P. Dendooven, H. Penttilä, K. Peräjärvi, A. Popov, and J. Aystö. Characterization of a cryogenic ion guide at igisol. *Nuclear Instruments and Methods in Physics Research*, 685:70–77, September 2012.

# Appendices

## A Chamber pressure vs gas cell pressure for He

### A.1 Chamber pressure vs gas cell pressure for He without skimmer and gas cell nozzle size $d_{nozzle} = 1.2$ mm.

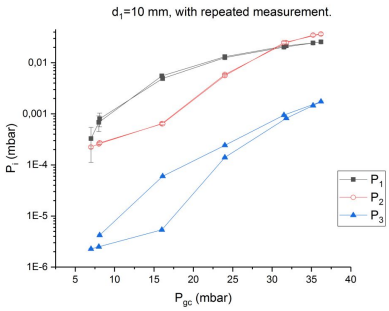


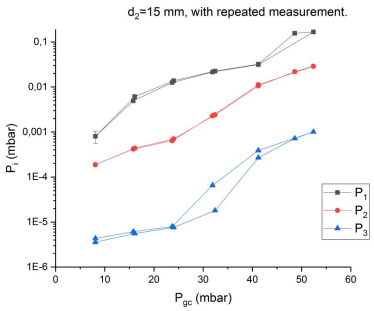


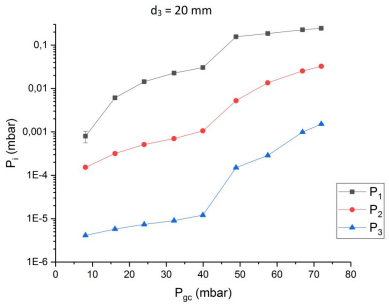


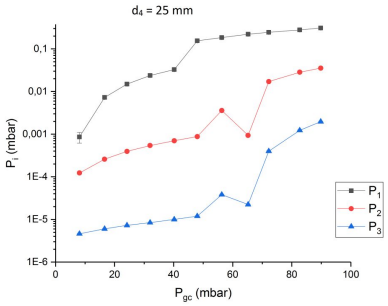


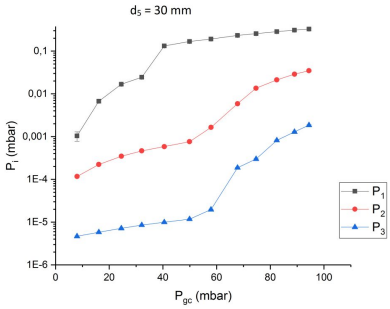


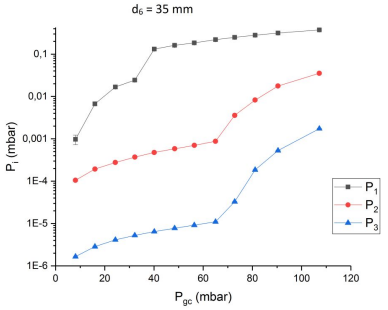

## A.2 Chamber pressure vs gas cell pressure for He with skimmer and gas cell nozzle size $d_{nozzle} = 0.5$ mm.

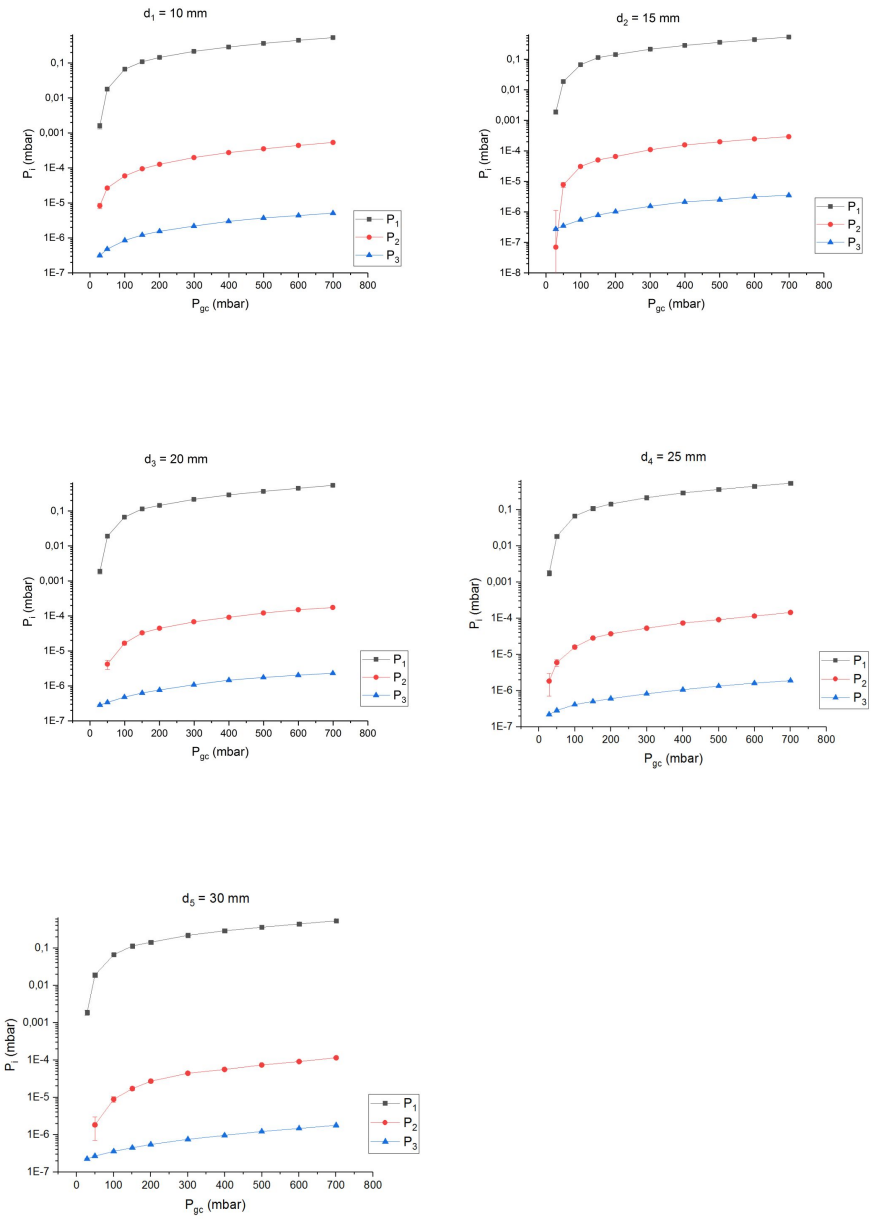

## A.3 Chamber pressure vs gas cell pressure for He with skimmer and gas cell nozzle size $d_{nozzle} = 0.9$ mm.

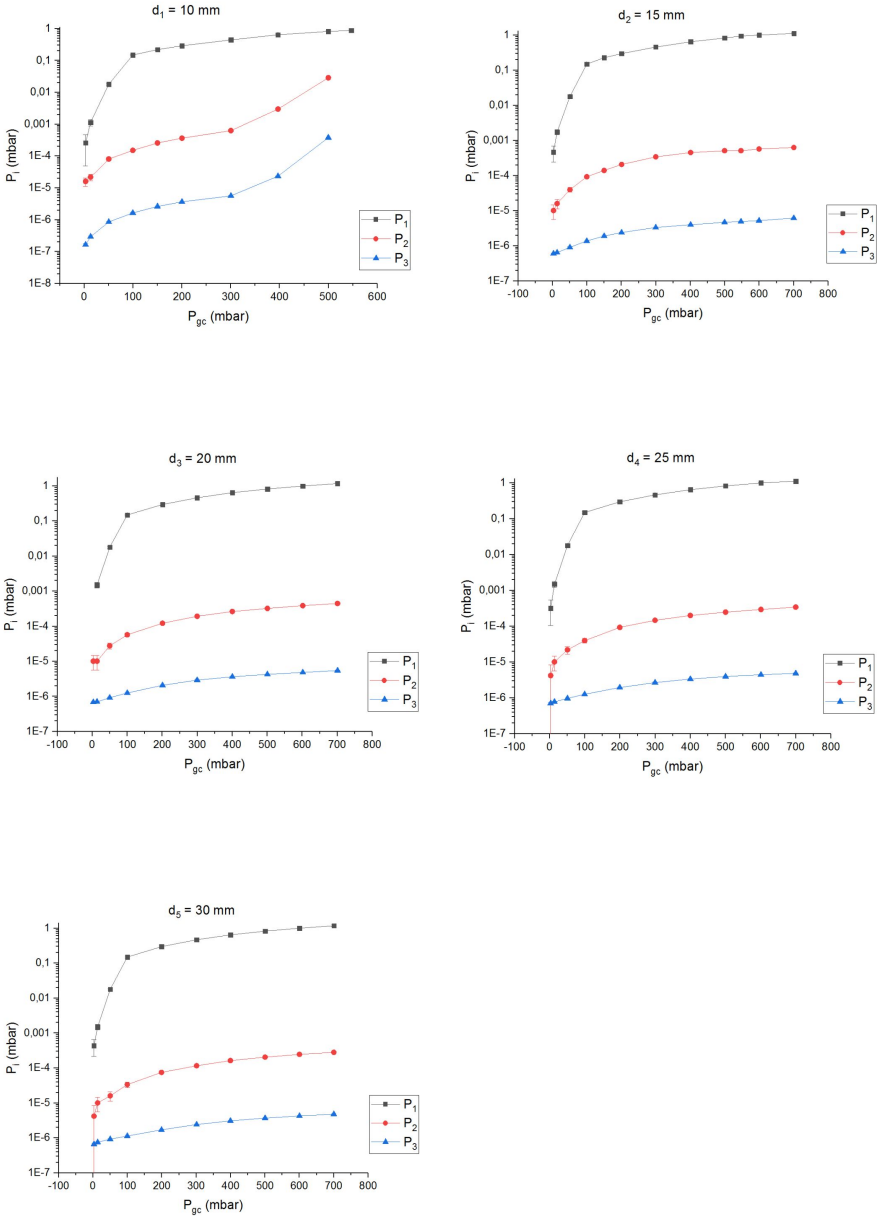

## A.4 Chamber pressure vs gas cell pressure for He with skimmer and gas cell nozzle size $d_{nozzle} = 1.2$ mm.

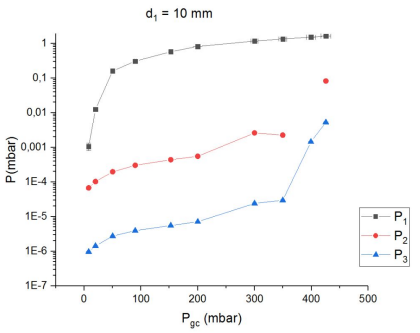


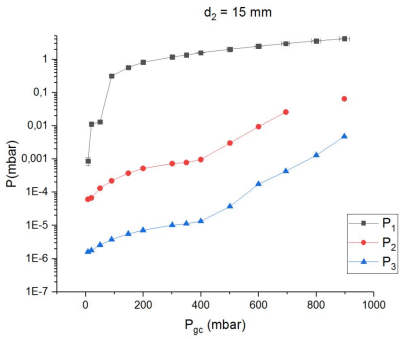


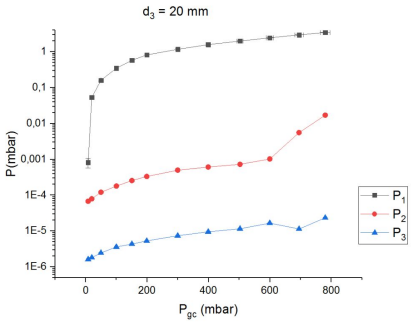


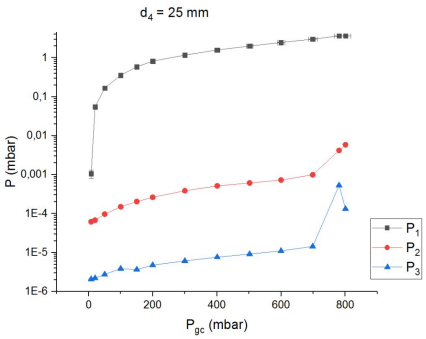


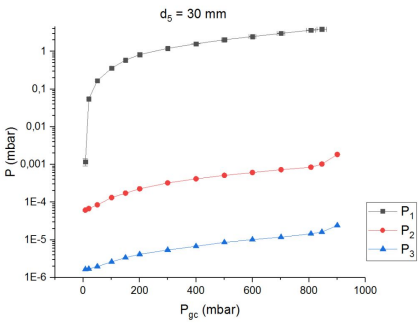

# B Chamber pressure vs gas cell pressure for Ar

## B.1 Chamber pressure vs gas cell pressure for Ar without skimmer and gas cell nozzle size $d_{nozzle} = 1.2$ mm.

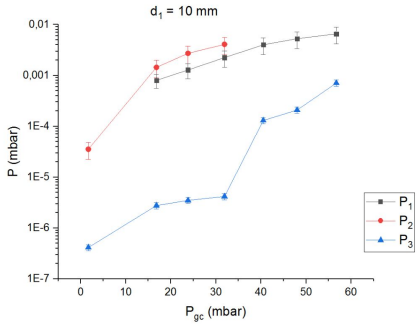


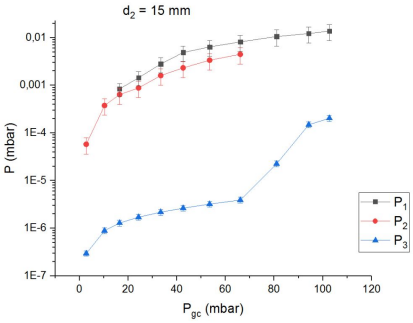


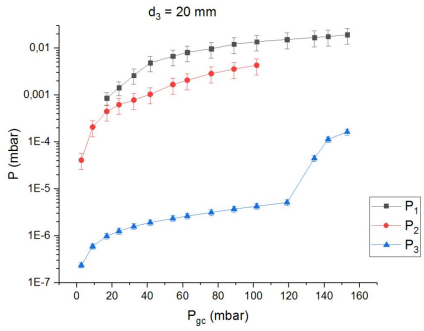


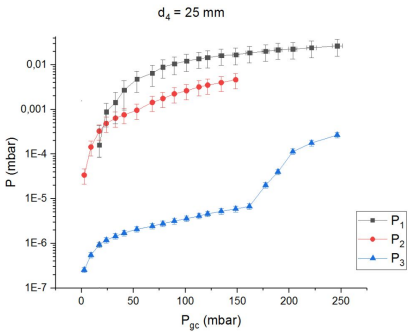


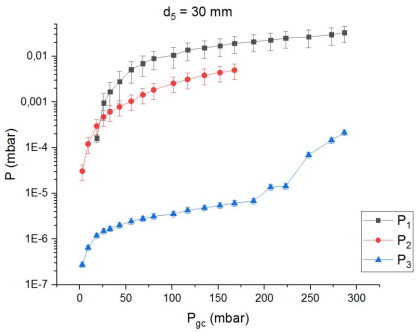


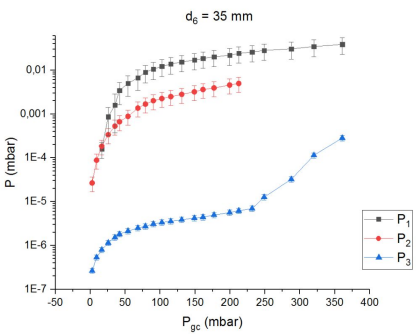

## B.2 Chamber pressure vs gas cell pressure for Ar with skimmer and gas cell nozzle size $d_{nozzle} = 0.5$ mm.

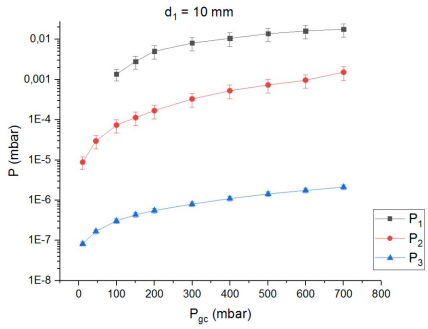


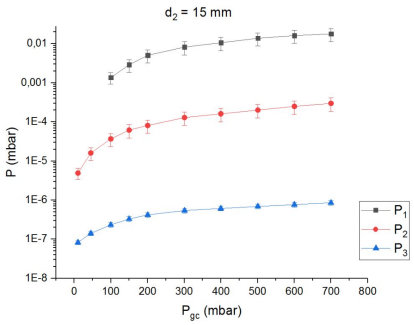


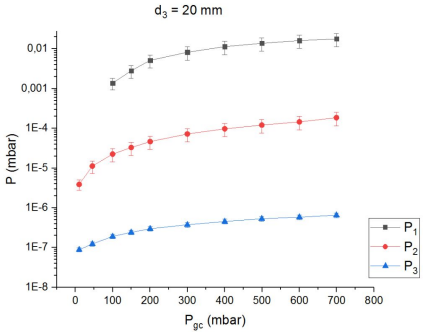


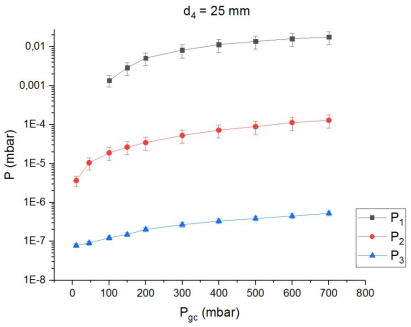


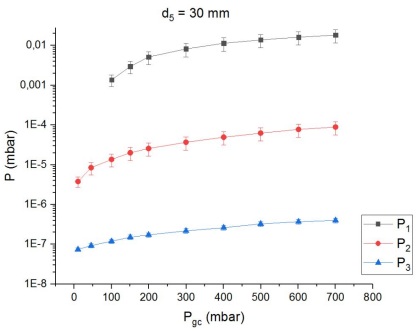

## B.3 Chamber pressure vs gas cell pressure for Ar with skimmer and gas cell nozzle size $d_{nozzle} = 0.9$ mm.

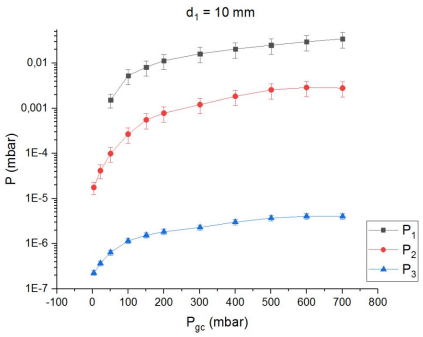


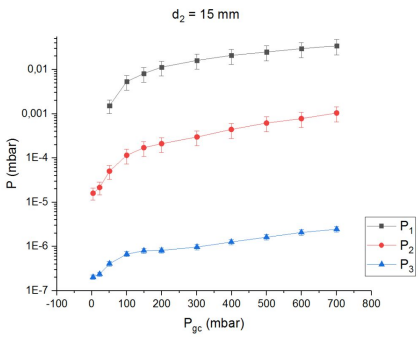


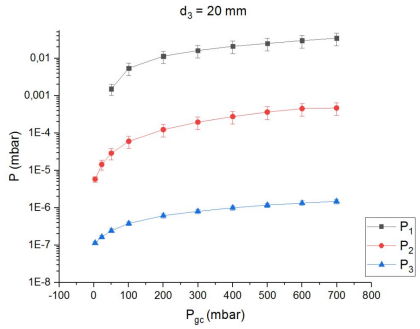


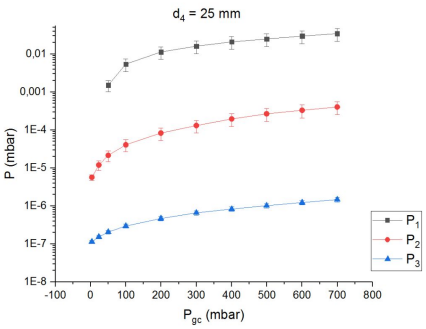


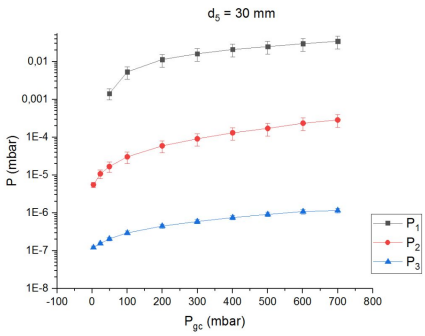

## B.4 Chamber pressure vs gas cell pressure for Ar with skimmer and gas cell nozzle size $d_{nozzle} = 1.2$ mm.

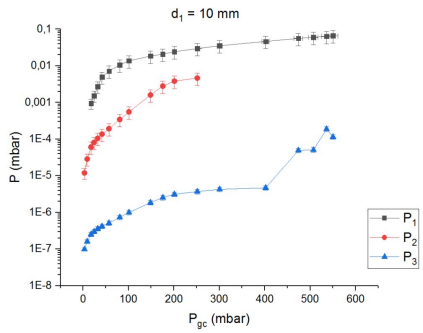


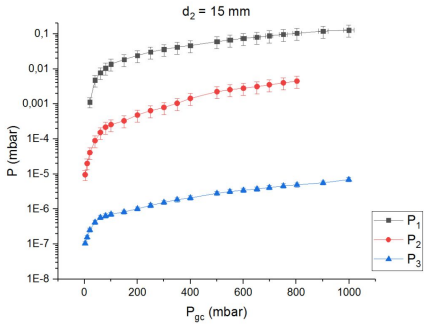


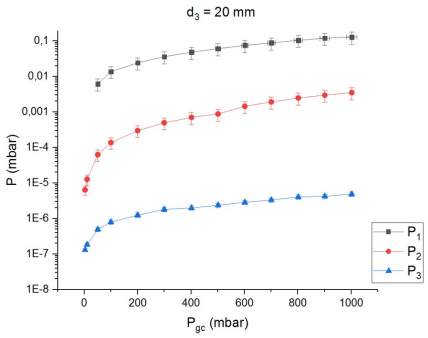


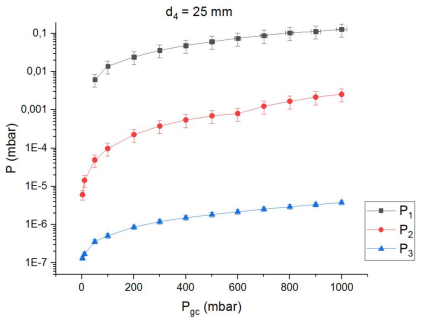


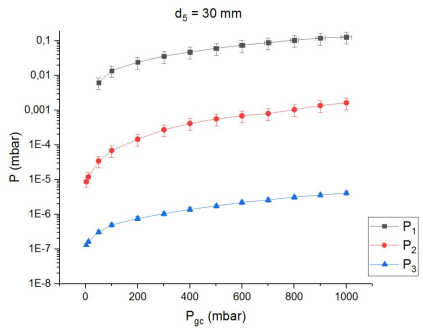

# C Alpha decay spectra at different gas cell pressures

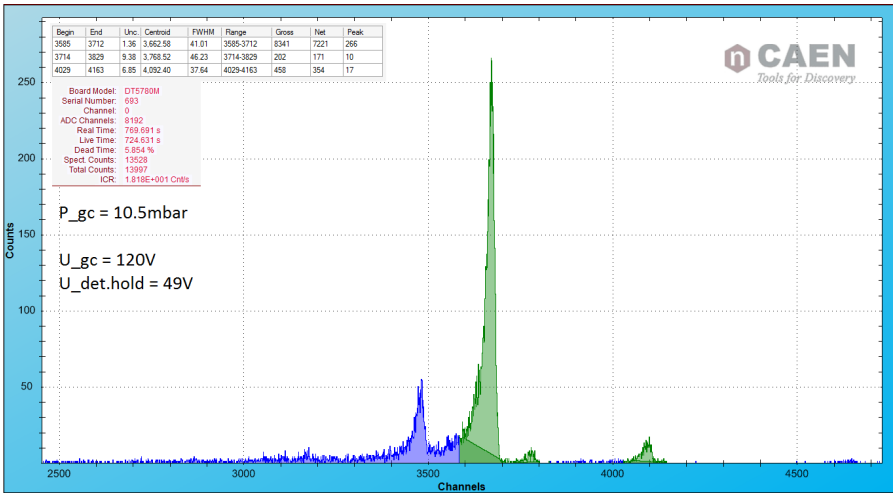


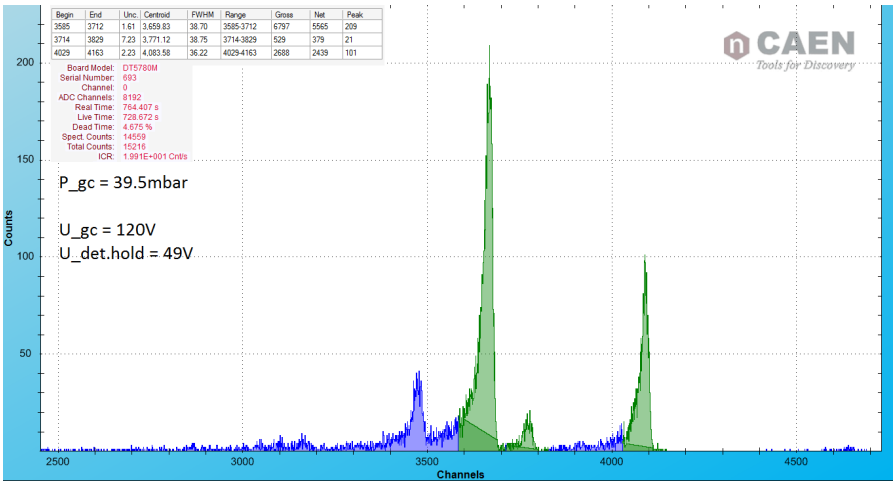

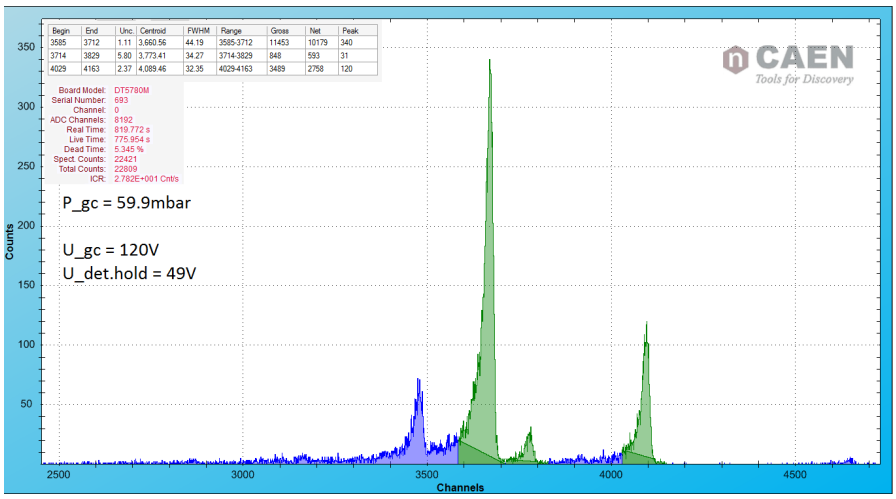
Begin End Unc. Centroid FWHM Range Gross Net Peak
3585 3712 1.11 3,660.56 44.19 3585-3712 11453 10179 340
3714 3829 5.80 3,773.41 34.27 3714-3829 848 593 31
4029 4163 2.37 4,089.46 32.35 4029-4163 3489 2758 120
Board Model: DT5780M
Serial Number: 693
Channel: 0
ADC Channels: 8192
Real Time: 819.772 s
Live Time: 775.954 s
Dead Time: 5.345 %
Spect. Counts: 22421
Total Counts: 22809
ICR: 2.782E+001 Cnt/s
P_gc = 59.9mbar
U_gc = 120V
U_det.hold = 49V
CAEN
Tools for Discovery
Counts
Channels
350
300
250
200
150
100
50
2500
3000
3500
4000
4500

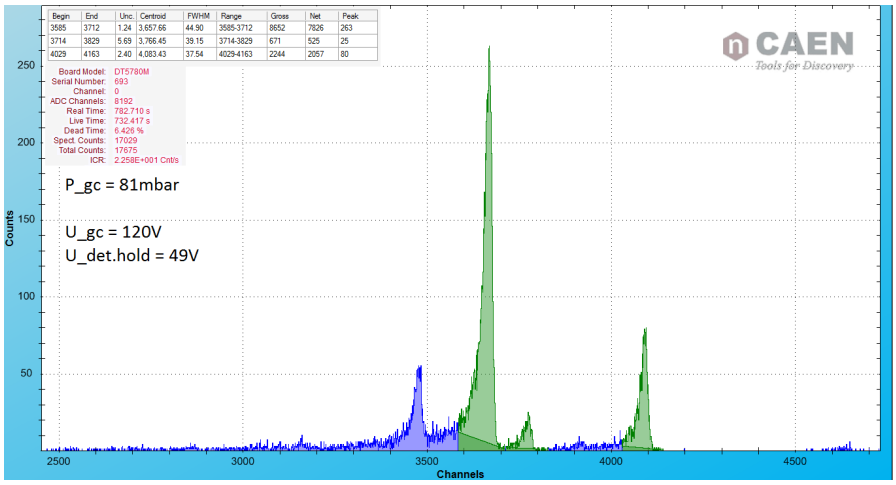
Begin End Unc. Centroid FWHM Range Gross Net Peak
3585 3712 1.24 3,657.66 44.90 3585-3712 8652 7826 263
3714 3829 5.69 3,766.45 39.15 3714-3829 671 525 25
4029 4163 2.40 4,083.43 37.54 4029-4163 2244 2057 80
Board Model: DT5780M
Serial Number: 693
Channel: 0
ADC Channels: 8192
Real Time: 782.710 s
Live Time: 732.417 s
Dead Time: 6.426 %
Spect. Counts: 17029
Total Counts: 17675
ICR: 2.258E+001 Cnt/s
P_gc = 81mbar
U_gc = 120V
U_det.hold = 49V
CAEN
Tools for Discovery
Counts
Channels
250
200
150
100
50
2500
3000
3500
4000
4500

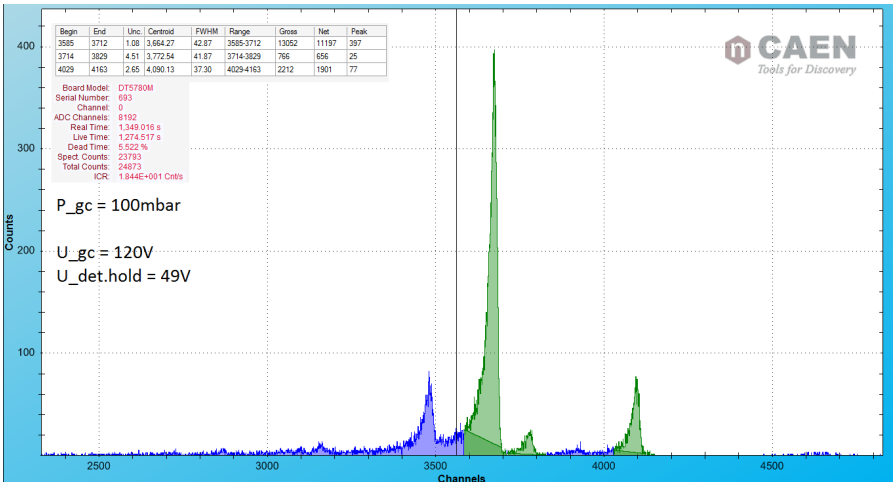
Begin End Unc. Centroid FWHM Range Gross Net Peak
3585 3712 1.08 3,664.27 42.87 3585-3712 13052 11197 397
3714 3829 4.51 3,772.54 41.87 3714-3829 766 656 25
4029 4163 2.65 4,090.13 37.30 4029-4163 2212 1901 77
Board Model: DT5780M
Serial Number: 693
Channel: 0
ADC Channels: 8192
Real Time: 1,349.016 s
Live Time: 1,274.517 s
Dead Time: 5.522 %
Spect. Counts: 23793
Total Counts: 24873
ICR: 1.844E+001 Cnt/s
P_gc = 100mbar
U_gc = 120V
U_det.hold = 49V
CAEN
Tools for Discovery
Counts
Channels
100
200
300
400
2500
3000
3500
4000
4500

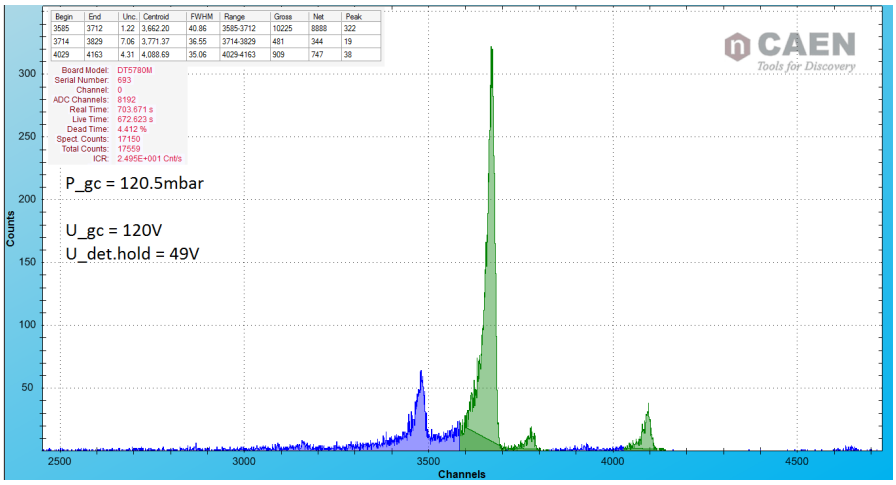
Begin End Unc. Centroid FWHM Range Gross Net Peak
3585 3712 1.22 3,662.20 40.86 3585-3712 10225 8888 322
3714 3829 7.06 3,771.37 36.55 3714-3829 481 344 19
4029 4163 4.31 4,088.69 35.06 4029-4163 909 747 38
Board Model: DT5780M
Serial Number: 693
Channel: 0
ADC Channels: 8192
Real Time: 703.671 s
Live Time: 672.623 s
Dead Time: 4.412 %
Spect. Counts: 17150
Total Counts: 17559
ICR: 2.495E+001 Cnt/s
P_gc = 120.5mbar
U_gc = 120V
U_det.hold = 49V
CAEN
Tools for Discovery
Counts
Channels
50
100
150
200
250
300
2500
3000
3500
4000
4500

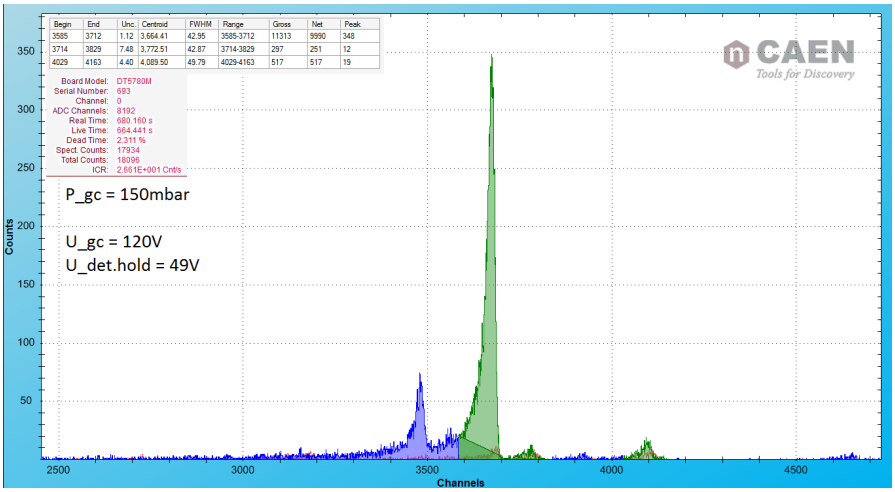
Begin End Unc. Centroid FWHM Range Gross Net Peak
3585 3712 1.12 3,664.41 42.95 3585-3712 11313 9990 348
3714 3829 7.48 3,772.51 42.87 3714-3829 297 251 12
4029 4163 4.40 4,089.50 49.79 4029-4163 517 517 19
Board Model: DT5780M
Serial Number: 693
Channel: 0
ADC Channels: 8192
Real Time: 680.160 s
Live Time: 664.441 s
Dead Time: 2.311 %
Spect. Counts: 17934
Total Counts: 18096
ICR: 2.661E+001 Cnt/s
P_gc = 150mbar
U_gc = 120V
U_det.hold = 49V
CAEN
Tools for Discovery
Counts
Channels
50
100
150
200
250
300
350
2500
3000
3500
4000
4500

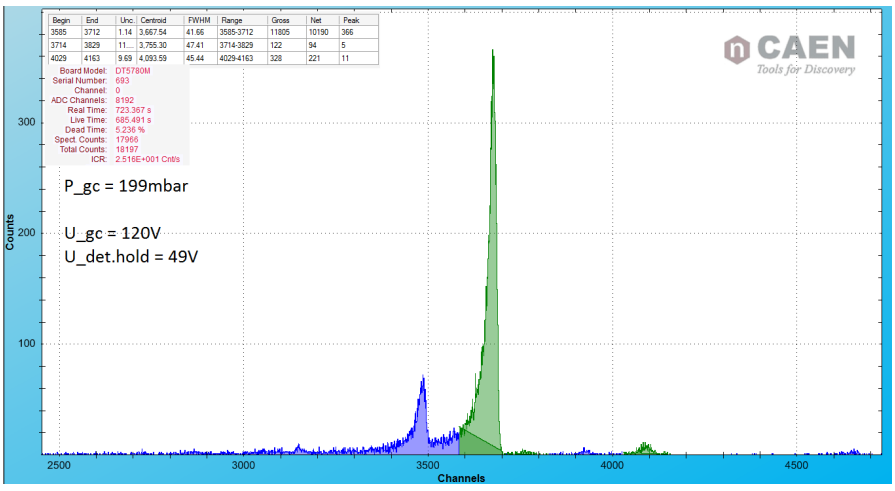
Begin End Unc. Centroid FWHM Range Gross Net Peak
3585 3712 1.14 3,667.54 41.66 3585-3712 11805 10190 366
3714 3829 11... 3,755.30 47.41 3714-3829 122 94 5
4029 4163 9.69 4,093.59 45.44 4029-4163 328 221 11
Board Model: DT5780M
Serial Number: 693
Channel: 0
ADC Channels: 8192
Real Time: 723.367 s
Live Time: 685.491 s
Dead Time: 5.236 %
Spect. Counts: 17966
Total Counts: 18197
ICR: 2.516E+001 Cnt/s
P_gc = 199mbar
U_gc = 120V
U_det.hold = 49V
CAEN
Tools for Discovery
Counts
Channels
100
200
300
2500
3000
3500
4000
4500

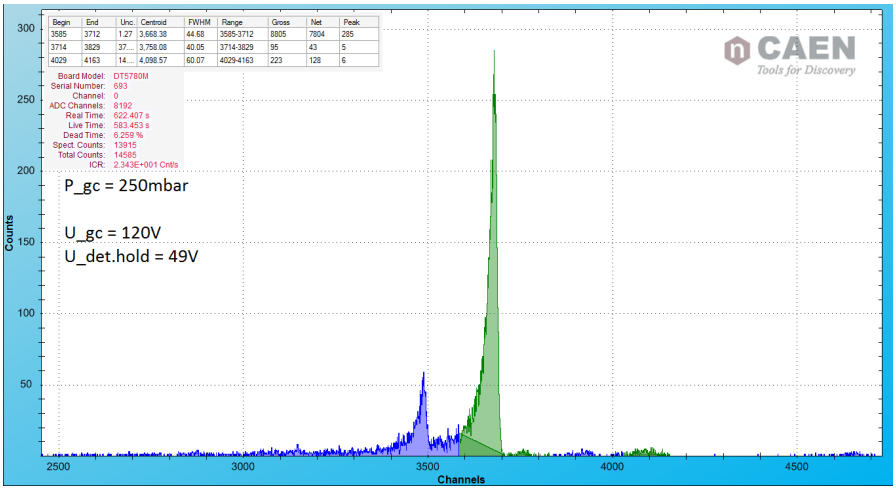
Begin End Unc. Centroid FWHM Range Gross Net Peak
3585 3712 1.27 3,668.38 44.68 3585-3712 8805 7804 285
3714 3829 37... 3,758.08 40.05 3714-3829 95 43 5
4029 4163 14... 4,098.57 60.07 4029-4163 223 128 6
Board Model: DT5780M
Serial Number: 693
Channel: 0
ADC Channels: 8192
Real Time: 622.407 s
Live Time: 583.453 s
Dead Time: 6.259 %
Spect. Counts: 13915
Total Counts: 14585
ICR: 2.343E+001 Cnt/s
P_gc = 250mbar
U_gc = 120V
U_det.hold = 49V
CAEN
Tools for Discovery
Counts
300
250
200
150
100
50
2500
3000
3500
4000
4500
Channels